

**An experimental study of bubbles and droplets rising
in a nematic liquid crystal**

by

Siddharth Khullar

A THESIS SUBMITTED IN PARTIAL FULFILLMENT OF THE REQUIREMENTS FOR
THE DEGREE OF

MASTER OF APPLIED SCIENCE

in

THE FACULTY OF GRADUATE STUDIES

(Chemical and Biological Engineering)

THE UNIVERSITY OF BRITISH COLUMBIA

August 2007

© Siddharth Khullar, 2007

ABSTRACT

Liquid crystals are nature's beautiful examples of complex materials which are fundamentally fascinating. Their unusual properties have intrigued researchers from a wide variety of fields including biologists, engineers, and even cosmologists.

This thesis focuses on the dynamics of topological defects occurring near micro-droplets and micro-bubbles as they rise through an aligned nematic liquid crystal. The experiments were conducted in a fabricated flow-cell, and the observations were made using polarized light microscopy with the help of a motion control system.

The results settle a controversy in the literature regarding the effect of hydrodynamic flow on the motion of defects by providing direct evidence of downstream convection of a Saturn ring defect and its transformation to a hyperbolic point defect. The point defect is convected further in the wake of the drop or bubble as the rising velocity increases. In equilibrium, both defect configurations may persist for long times. But the point defect sometimes spontaneously opens into a Saturn ring, indicating the latter as the globally stable configuration for the conditions used. A quantitative analysis of the rise velocities versus the location of defects yields graphs which are consistent with recent theoretical predictions. Besides these, we also observe interesting multiple drop and bubble interactions leading to the phenomenon of self-assembly and distorted defect structures.

ACKNOWLEDGEMENTS

First, I want to express my heartfelt gratitude to my supervisor Prof. James Feng under whose guidance this work saw its completion. His encouragement and support provided a solid ground on which I could execute my research. He taught me the skill of scientific writing and organised approach to problem solving, which I believe to be the vital ingredients for intellectual research.

I would like to extend my thanks to my committee members – Dr. Boris Stoeber and Dr. Royann Petrell who carefully oversaw the completion of this project. Dr. Stoeber's ideas during the setting of my experiments were of valuable assistance and Dr. Petrell's captivating talks about her everyday experiences kept me going on enthusiastically. I appreciate Chunfeng Zhou's help and contribution to this project. I had many interesting chats with him as an officemate. During the initial stages, I enjoyed working with Xiaopeng (Paul) Chen, whose guidance helped me adjust with ease. I am grateful to Dr. Teodor Burghilea for his help in setting up of my experiment. I also appreciate Prof. John Gosline's and Prof. Robert Shadwick's efforts to help us with the imaging system.

I owe many thanks to all of my friends, especially Raghavendra and Pramod for their support and suggestions. I want to thank my family members for keeping up my morale, throughout my masters' programme. My mom deserves a special mention for taking care of me through all these years, and her unfailing belief in my abilities. It is because of her scientific aptitude and diligence that kindled my liking towards science.

I appreciate our department faculty and staff for their cooperation and assistance.

TABLE OF CONTENTS

ABSTRACT	ii
ACKNOWLEDGEMENTS	iii
TABLE OF CONTENTS	iv
LIST OF FIGURES	vi
LIST OF TABLES	ix
1 INTRODUCTION	1
1.1 Discovery of Liquid Crystals (LCs).....	1
1.2 Description of LCs.....	1
1.3 LC Nomenclature.....	3
1.3.1 The director	3
1.3.2 The order parameter	3
1.3.3 Anchoring (surface alignment)	4
1.3.4 Elasticity and Free energy.....	6
1.4 Defects in Liquid crystals	6
1.5 Hyperbolic point and ring defects.....	8
1.6 Stability of Defects	9
1.6.1 Effect of particle size	9
1.6.2 Effect of External fields.....	11
1.6.3 Effect of flow	13
1.7 Objective and Scope of this thesis	14
2 EXPERIMENTAL MATERIALS AND METHODS	15
2.1 Observation of Liquid Crystals.....	15
2.2 Polarized light	15
2.2.1 Light Propagation through a liquid crystalline medium	16
2.3 Quantitative Imaging using Abrio	17
2.3.1 Restriction imposed by Abrio	18
2.4 Schlieren Texture	19
2.5 Cell fabrication and preparation.....	22
2.6 Uniform Planar Wall Anchoring.....	23
2.7 Anchoring at 5CB-air interface.....	25
2.8 Motion Control System and microscope.....	26

2.9	Micro-bubble and micro-drop production	28
2.10	Rising bubble in homeotropically wall anchored cell.....	29
2.11	Materials used and their properties	33
3	RESULTS	35
3.1	Defects on static bubbles and droplets.....	35
3.1.1	Comparison with computed profile	36
3.1.2	Comparison with quantitative imaging using Abrio.....	37
3.1.3	Spontaneous and induced point defect to Saturn-ring transition	39
3.2	Oil drops in motion	41
3.3	Air bubbles in motion	45
3.3.1	Elastic relaxation.....	47
3.3.2	Loop breaking	48
3.4	Multi particle interactions.....	49
3.4.1	Self assembly among micro-droplets and micro-bubbles.....	49
3.4.2	Deformed defect structures.....	51
3.5	Conclusions.....	53
3.6	Recommendations for future work	54
4	REFERENCES.....	56
5	APPENDIX.....	60
5.1	Structure and properties of 5CB	60
5.2	Abrio's Working Layout.....	61
5.3	Abrio's Specifications.....	62

LIST OF FIGURES

Figure 1: A pictorial representation of molecular organization in different phases	2
Figure 2: An illustration depicting the director (shown by the arrow) and the meaning of order parameter in liquid crystals	4
Figure 3: Anchoring phenomenon in liquid crystals. The arrow shows the anchoring direction..	5
Figure 4: Geometric arrangement of the director leading to hyperbolic and radial types of point defects.	7
Figure 5: Schematic showing the director profile of a hyperbolic satellite point defect (a) and a Saturn-ring defect (b), surrounding a particle with homeotropic anchoring at its surface. The orientation is vertical in the far field.....	8
Figure 6: Schlieren pattern in a thin sample of liquid crystal (no wall anchoring) as seen through crossed polarizers (a) , and the corresponding Abrio snapshot (b) with the superimposed orientation vectors.....	21
Figure 7: Schematic of a fabricated cell	23
Figure 8: Schematic showing the direction of light path through the plane of observation (X-Y) in a wedged cell.	24
Figure 9: Abrio snapshot of a wedged cell leading to the appearance of retardance bands.	24
Figure 10: Crossed polarizers image (a) and the corresponding Abrio snapshot (b) of a thin drop of LC placed on a glass slide.	25
Figure 11: Abrio snapshot of a 5CB film sitting on a single glass slide exposed to air. The intensity indicates the measured retardance and the superimposed vectors represent the LC-director. Note that the abrupt and repetitive 90 degree turns in the vectors is due to a restriction in Abrio's working and is to be correctly interpreted by rotating through 90 degrees, as mentioned before. The anchoring near air-LC interface is homeotropic.....	26
Figure 12: Schematic of the experimental setup.....	27
Figure 13: A photograph showing the experimental setup	28
Figure 14: Schematic of a bubble rising in a cell with homeotropic wall anchoring. The anchoring at the bubble surface being homeotropic, will lead to a relaxed director (shown in red) profile.....	31
Figure 15: A bubble moving in a cell with homeotropic wall anchoring (a) Retardance intensity Abrio snapshot; (b) False colour azimuth profile with superimposed orientation vectors; (c) Retardance vs distance plot.....	32

Figure 16: Schematic of a drop/bubble with homeotropic anchoring in a cell with planar wall anchoring. One of the polarizer's optic axis (P) is parallel to the alignment direction and the other polarizer (A) is crossed at 90 degrees to the first one. Light path is indicated by the arrows.	35
Figure 17: Static defects surrounding oil drops as viewed through crossed polarizers. (a) Saturn-ring defect (drop radius $a = 30.2 \mu\text{m}$); (b) point defect ($a = 21.8 \mu\text{m}$); (c) computed director field and light intensity graph for a point defect.	36
Figure 18: Abrio snapshot (b) of an oil droplet possessing a dipolar point defect with the corresponding crossed polarizers' image (a). The white vectors represent the measured orientation profile. The red lines are the superimposed edited director orientations, some of which are turned by 90° whenever the retardance falls outside the measurable range (as discussed in section 2.3.1). The LC - drop interface is demarcated by the black circular ring.	38
Figure 19: Spontaneous point-to-ring transformation around a stationary bubble of radius $a = 100 \mu\text{m}$. The images were taken through crossed polarizers, and (a) shows the characteristic birefringence pattern for the point defect (cf. Figure 17(c)).	39
Figure 20: Time series of snapshots showing convection of a Saturn-ring defect (present around a rising oil droplet) and its ultimate convergence to a steady state point defect. The images were taken with single polarizer for clarity.	43
Figure 21: (a) Position of the ring or point defect as a function of Ericksen number ($Er = \eta va/K$) oil droplet run of Figure 20. For the Saturn ring (squares), r_d is the vertical distance between the drop center and the edge of the ring. For the satellite point defect (circles), r_d is the distance from the drop center. $A = 15.1$. The inset shows the velocity overshoot that coincides with the ring-to-point transition. Arrows A and B correspond to the first and last data points in the inset; (b) Numerical prediction of steady-state defect positions for $A = 30$, after Fig. 7 of [Zhou et al. 2007], ©Cambridge University Press.	44
Figure 22: Position of the point defect as a function of the instantaneous Ericksen number (Er) for accelerating and decelerating bubbles. Insets B1 and B2 show the bright birefringent loops with the point defect at the bottom, and C shows a computed birefringent pattern roughly corresponding to B2. The solid arrow indicates the final stabilization of the point defect to its equilibrium position (inset A).	46
Figure 23: Time series (a) - (e) of the elastic retraction process on a static bubble. The instantaneous loop retraction velocities (v_{loop}) are given except for (b) which is the start of a new reference frame.	47

Figure 24: Annihilation of a pair of opposite point defects with opposite charges. The length of the loop shrinks at a rate of $27.4 \mu\text{m/s}$, so that each point defect moves at a speed of $13.7 \mu\text{m/s}$. The scale bar in (a) corresponds to $100 \mu\text{m}$.	48
Figure 25: Self-assembly of oil droplets in LC medium. The droplets are in the size range of ≈ 5 to 10 microns.	50
Figure 26: Self assembly at a large scale. Air bubbles, $\approx 100 \mu\text{m}$ in diameter, self assembling in vertically aligned liquid crystal.	51
Figure 27: Deformed defect structure can be observed between a pair of static air bubbles in (a) and (b) above. Another pair of static bubbles (c) at separation distance $d \approx 10a$ form a stretched-gum type of defect	52
Figure 28: Molecular representation of liquid crystal 5CB	60

LIST OF TABLES

Table 1: Material properties	33
Table 2: Additional properties of 5CB.....	60

1 INTRODUCTION*

1.1 Discovery of Liquid Crystals (LCs)

The discovery of liquid crystals dates back to more than 150 years ago when Virchow, Mettenheimer and Valentin found that a compound from the nerve core exhibited strange behaviour when viewed with polarizing light. Not realizing the uniqueness of this new phase, they labelled the compound as a 'living crystal'. However, the official discovery of liquid crystals is credited to Otto Lehmann, a German physicist and Friedrich Reinitzer, an Austrian botanist. Reinitzer, while conducting experiments on an organic compound named cholesteryl benzoate, was surprised by the fact that it had two melting points. At 145.5 °C the solid crystal melted into a cloudy liquid which existed until 178.5 °C where the cloudiness suddenly disappeared, giving way to a clear transparent liquid. Puzzled by this mysterious behaviour, he turned to Lehmann who confirmed his findings and later coined the term 'liquid crystal', indicating a state with properties between a liquid and a solid. This idea of a new fourth state of matter was disputed by the scientific community, but was accepted a few decades later with numerous reports and conclusive experiments of liquid crystalline behaviour becoming prevalent.

Liquid crystals' use for display applications was developed in 1960's thus fuelling an increased research focus in every aspect of liquid crystal science involving chemists, physicists, applied scientists and engineers. Today, these materials are at the core of many technological innovations among which liquid crystal displays and liquid crystal thermometers are the best known. Liquid crystal displays make use of a thin sample of twisted liquid crystal sandwiched between crossed-polarizers. By applying an electric field, the pixels comprising of individual liquid crystal cells can be made to act as a light valve, thus controlling the on-off state of individual pixel.

1.2 Description of LCs

Liquid crystals' fundamental unit is called a 'mesogen'. Mesogen, which is derived from Greek, meaning 'species in between', illustrates the idea that the liquid crystalline state behaves in a

* A version of this thesis has been submitted for publication [Khullar et al. 2007].

manner which is intermediate between crystalline solids and amorphous liquids. Owing to the molecules' anisometric shape (rod-like and disc-like being the most common) and their non-covalent interactions, a gamut of interesting properties differentiate these from conventional solids or liquids. These include the ability of molecules to orient collectively, spontaneously or in the presence of electric or magnetic field and to anchor preferentially to a binding surface, and the optical property of birefringence among others.

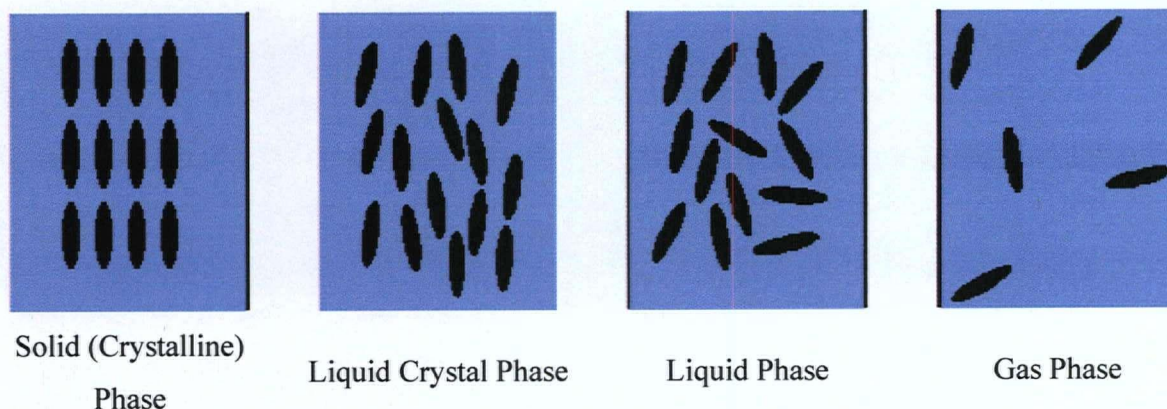


Figure 1: A pictorial representation of molecular organization in different phases

Figure 1 shows a comparison of molecular order among different phases. Crystalline solids have orientational as well as positional order. Liquids have neither orientational nor positional order. In between these two, are liquid crystals, which have orientational order but partial or no positional order.

Liquid crystalline molecules fall into two groups: thermotropes and lyotropes. Thermotropic liquid crystals or thermotropes, are characterized by the presence of phase transitions which depend on temperature. In general, a temperature change can induce a transition from solid crystalline phase to liquid crystal phase and further to an isotropic phase. Inside the liquid crystal phase, the strength of intermolecular interactions is a direct function of the temperature.

Lyotropic compounds, on the other hand, exhibit liquid crystalline behaviour when dissolved in proper solvents and the state is concentration dependent. For example, amphiphilic molecules consisting of a short polar head with a long polar tail (as in surfactants), when dissolved in water, may exhibit liquid crystalline behaviour. At critical concentrations these aggregate into specialized structures giving rise to vesicles and micelles. Solutions of polypeptide enantiomers

like polybenzyl-L-glutamate (PBLG) and polybenzyl-D-glutamate (PBDG) also add to the class of lyotropic liquid crystals.

Liquid crystals can also be classified according to molecular size, into small molecule and polymeric liquid crystals. Either can be thermotropic or lyotropic [Collings and Hird 1997]. For polymeric liquid crystals, the mesogenic unit is incorporated into the main chain or side chain of a polymer, thus combining the properties of polymers and liquid crystals. Another special class of polymer liquid crystal consists of molecules (typically biological) suspended in high concentrations, an example being the tobacco mosaic virus. Colloidal suspensions of this rod shaped virus exhibit liquid crystalline phases, such as the nematic and smectic phases.

1.3 LC Nomenclature

Liquid crystals come in different flavours, which can be distinguished by the dimensionality of translational order. Nematic phases have no translational order while smectic, columnar and other phases can have single or multi-dimensional translational orders. Here, we will be concerned with the nematic phase only.

1.3.1 The director

The director, represented by the unit vector \mathbf{n} , denotes the average of the directions carried by individual molecules over a volume V , which is large compared to the molecular dimensions but small with respect to typical distortion lengths in the nematic. Figure 2 illustrates an arrangement of rod-like molecules for which the director \mathbf{n} can be drawn (shown by the arrow). The molecular arrangement remains symmetric even when the molecules are flipped over, thus keeping the director the same. For this reason \mathbf{n} and $-\mathbf{n}$ are equivalent i.e. $\mathbf{n} \equiv -\mathbf{n}$. The director can be defined at all points in the sample except at singularities (or regions of defects).

1.3.2 The order parameter

The order parameter helps describe the long-range order of properties (thermodynamic or structural) which repeat uniformly in a system. For liquid crystals, it is easy to convince oneself that a nematic state will be more ordered than the isotropic phase. The degree of orientational order can be measured in terms of the order parameter s , first introduced by Tsvetkov [1942]:

$$s = \frac{1}{2} \langle 3 \cos^2 \theta - 1 \rangle \quad (1)$$

where, θ is the angle between the mesogen's long molecular axis and the preferred orientation direction \mathbf{n} , and the angular brackets denote an average over all molecular orientations (see Figure 2). In a perfect alignment case (most ordered state) $s = 1$, while for most randomly ordered state (isotropic phase) $s = 0$. In liquid crystalline state, s lies between 0 and 1. For thermotropes, s has a strong temperature dependency in the nematic phase.

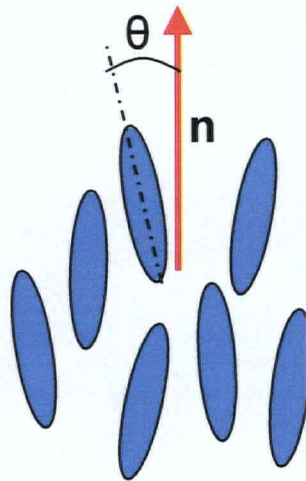


Figure 2: An illustration depicting the director (shown by the arrow) and the meaning of order parameter in liquid crystals.

1.3.3 Anchoring (surface alignment)

When a nematic phase comes in contact with another phase (solid, liquid or gas), an interface is created. Close to the interface, the nematic molecules take a fixed mean orientation which is transmitted into the bulk phase via elastic forces. This ability of the liquid crystal molecules to bind and align preferentially to a surface is known as anchoring (Figure 3). It is analogous to the phenomenon of ‘epitaxy’ of solids on substrates. The anchoring direction in liquid crystals is determined by the choice of surface in contact and can be controlled by mechanical and chemical treatments of the substrate. Perpendicular anchoring occurs when the molecules align perpendicular to the surface. It is also known as homeotropic anchoring. When the molecules lie ‘flat’ in the plane of the surface in contact, it is called planar anchoring. The molecules can also occupy positions oblique to the surface in which case it is known as tilted anchoring. In reality

there is no rigid homeotropic or planar anchoring, as there will always be some small deviations in the angle which the molecules make with the surface.

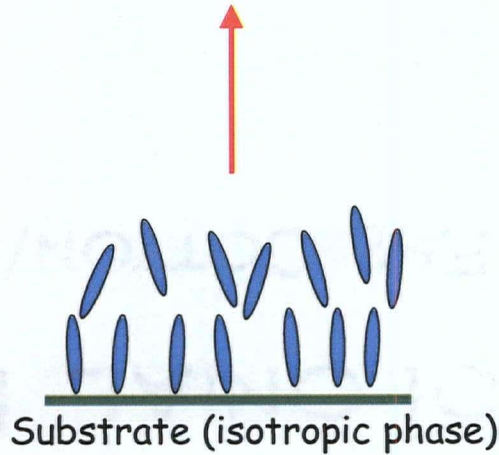


Figure 3: Anchoring phenomenon in liquid crystals. The arrow shows the anchoring direction.

An anchoring strength can be described in terms of polar (θ) and azimuthal (φ) deviations of the molecular orientation from the anchoring direction (also called easy axis). Often the anchoring energy function, w , is written as [Kleman and Lavrentovich 2003]:

$$w = \frac{1}{2} w_{\theta} (\theta - \theta_0)^2 \quad \text{or} \quad w = \frac{1}{2} w_{\varphi} (\varphi - \varphi_0)^2 \quad (2)$$

where, (θ_0, φ_0) define the equilibrium director orientation. The coefficients of proportionality w_{θ} and w_{φ} are referred to as the polar and azimuthal anchoring energy coefficients, respectively. It indicates the energy penalty incurred when the director deviates from the preferred anchoring direction. The azimuthal anchoring coefficient (w_{φ}) is usually found to be one to two orders lower than its polar counterpart (w_{θ}) [Demus et al. 1999].

This kind of relationship with interfacial energy was first considered by Rapini and Papoular [1969], who postulated the polar part of the anchoring energy function to be of the form:

$$w = \frac{1}{2} w_{\theta} \sin^2(\theta - \theta_0) \quad (3)$$

For a liquid crystal in contact with an isotropic fluid, the anchoring energy is dependent only on the polar part and we may use W instead of w_0 .

1.3.4 Elasticity and Free energy

If the preferred orientation of the molecules (e.g., imposed by anchoring) in a region is disturbed (e.g., by application of magnetic field), the medium experiences an increase in the free energy of the system. For nematics, the free energy F per unit volume of the deformed state relative to the state of uniform orientation is expressed, in vector notation, as [Chandrasekhar 1992]:

$$F = \frac{1}{2} k_{11} (\nabla \cdot \mathbf{n})^2 + \frac{1}{2} k_{22} (\mathbf{n} \cdot \nabla \times \mathbf{n})^2 + \frac{1}{2} k_{33} (\mathbf{n} \times \nabla \times \mathbf{n})^2 \quad (4)$$

Here, \mathbf{n} is the director and $\nabla \cdot \mathbf{n}$, $\mathbf{n} \cdot \nabla \times \mathbf{n}$, $\mathbf{n} \times \nabla \times \mathbf{n}$ represent the three types of deformation components at any point, viz: *splay*, *twist* and *bend* respectively. k_{11} , k_{22} and k_{33} are known as the elastic constants for splay, twist and bend respectively.

Any type of deformation can be represented by a combination of these three types of basic conformations. Often times for simplicity, the one constant approximation is used, i.e. $k_{11} = k_{22} = k_{33} = K$. This is reasonable since the values of k 's are on the same order of magnitude for most liquid crystals.

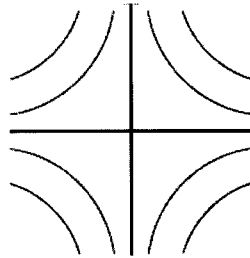
1.4 Defects in Liquid crystals

Defects are common in crystalline materials where they disrupt the regular pattern of atomic arrangement. Topological defects are a consequence of symmetry breaking in ordered systems such as liquid crystals. Their presence has been well documented in crystalline solids [Friedel 1964; Nabarro 1967] and can be found in systems as wide as superfluid helium [Vollhardt 1990] and cosmology [Chuang et al. 1991; Ray and Srivastava 2004].

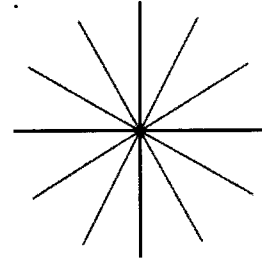
Liquid crystals show more complex (and a greater number) of defects than crystalline solids, ranging in dimensions from point defects to wall defects. Defects in liquid crystals can be thought of as discontinuities in the inclination of the director. The common disclinations (dislocations of rotation) found in uniaxial nematics are, line defects and point defects. At the disclination core the order parameter of the system is usually lowered and the nematic director

loses its meaning. There is even a possibility of the liquid crystal melting to an isotropic state at the defect core. A disclination produces a strong distortion in its neighbourhood leading to steep gradients in the director $\mathbf{n}(\mathbf{r})$, the effects of which penetrate the bulk of the system.

Figure 4 shows two examples of commonly found defect types in nematic liquid crystals. The lines represent the director field and the core of the defect is at the geometric center of the figures. The defects can be classified by assigning them a charge or strength, corresponding to the molecular arrangement around the defect core [de Gennes and Prost 1993]. In Figure 4, the hyperbolic hedgehog and radial defects have charges $Q = -1$ and $Q = +1$ respectively, indicating a respective rotation of the director when the disclination is encircled in the anticlockwise direction. Thus, if we follow a closed loop around the singularity making one full turn (2π), the director rotates by $2\pi Q$ leading to a defect of charge $= 2\pi Q / 2\pi$.



Hyperbolic hedgehog type defect of charge
 $Q = -1$



Radial defect of charge $Q = +1$

Figure 4: Geometric arrangement of the director leading to hyperbolic and radial types of point defects.

Defects can also occur at the domain boundaries in a liquid crystalline medium. If a liquid crystal has no imposed anchoring boundaries, its molecules may not point in the same direction at all points in the sample. This can lead to the formation of domains or localized regions in the sample in which the average orientation of molecules is the same. Normally, there will be numerous such domains in the sample. Often the director will change abruptly at places where these domains meet. At such locations, the liquid crystalline state relaxes thus nucleating a defect.

1.5 *Hyperbolic point and ring defects*

When an external agent or inclusion, placed inside a uniformly aligned bulk nematic, disturbs this uniformity (orientation order) by imposing its own set of anchoring conditions, the liquid crystal is forced to nucleate a defect in order to satisfy the boundary conditions. For example, if this inclusion is a spherical particle which imposes homeotropic anchoring at its surface, there are two possible defect configurations that can occur - a companion hyperbolic point defect or a Saturn-ring defect (see Figure 5). The hyperbolic point defect (carrying a charge -1), helps maintain charge neutrality of the system by compensating with the radial configuration of charge $+1$ imposed by the particle. The Saturn-ring consists of a line disclination ring of finite radius and charge $-1/2$ encircling around the particle. The Saturn-ring can occupy one of many positions offset from the equatorial plane of the particle and even be shrunk to a hyperbolic point defect at one of the poles, thus making it topologically equivalent with the latter. Note that a particle accompanying a hyperbolic point defect has dipolar symmetry while one with a Saturn-ring defect will have quadrupolar symmetry. The terms 'dipolar defect' and 'quadrupolar defect' may be used alone for the general case of defects having dipolar and quadrupolar symmetries respectively, especially where further information on defect type may not be known with certainty.



Figure 5: Schematic showing the director profile of a hyperbolic satellite point defect (a) and a Saturn-ring defect (b), surrounding a particle with homeotropic anchoring at its surface. The orientation is vertical in the far field.

In recent years, defects near an embedded particle or droplet have been the subject of extensive studies (see following section). Due to the topological equivalency of Saturn-ring and hyperbolic

point defects, an interesting question arises: Under what conditions will it be possible for one type of defect to be converted into the other? This has resulted in a large number of theoretical and experimental studies concerning the mutual stability of these two defect types. This tremendous attention has also been stimulated by the unusual behaviour of multi-particle interactions in liquid crystal medium which is different from the conventional colloidal systems*. As we shall see later, the anchoring constant W , bulk elastic constant K and the radius of particle a , play a crucial role in determining the stability of defect types. Hence, the ratio $A = Wa/K$ represents the competition between surface anchoring energy and bulk elasticity.

1.6 Stability of Defects

Out of the two possible defect configurations – the companion point defect and the Saturn-ring defect, neither one can be guaranteed to occur without further knowledge. The stability of either type essentially depends on the particle size and strength of surface anchoring. Other factors like magnetic field and hydrodynamic flow also play an important role in the stability. The following subsections summarize the important work done by others on the stability of these two defect configurations.

1.6.1 Effect of particle size

1.6.1.1 Computational

Typically, the stability of a defect structure is calculated by the minimization of the system's total free energy, which includes the Frank free energy F and a surface energy term to account for the anchoring at the particle's surface.

Stark's [2001] analysis of the stability predicts that, for small particle sizes (radius = 180 nm) the Saturn-ring possesses a lower free energy and thus has absolute stability. Above a radius of 720 nm, the dipolar defect becomes the global energy minimiser while the ring seems to enjoy meta-stability. These cannot be translated exactly to real scenario because of the various assumptions and parameters used, the most important ones among them being:

- a) Assumption of rigid anchoring of director on particle's surface ($W \rightarrow \infty$)

* See section 3.4.1 for further details

- b) The calculated particle size depends on the assumed core size of the defect and the line energy of the disclination.

Numerical investigations by Ruhwandl and Terentjev [1997] concluded that both, Saturn-ring and dipolar satellite defect are possible, their stability depending on Wa/K , the relative strength of director anchoring at the surface versus the bulk elasticity. Also, the transition from one state to another would be difficult owing to a high and wide energy barrier of the order of $1000 k_b T$; k_b being the Boltzmann constant (1.381×10^{-23} J/K) and T is the temperature. For numerically calculated values of $Wa/K \approx > 10$, both ring and satellite point defects are stable solutions with the satellite enjoying somewhat lower energy than the ring, although the estimate is not concrete. This energy difference lessens as the value of Wa/K decreases, indicating that Saturn-ring may be unfavourable for larger particles.

The Frank theory cannot resolve the defect cores. Hence for using Frank theory throughout the sample region, the defect cores are typically assigned an energy value, which is then added to the free energy F . This yields results which are highly dependent on defect size and the core energy, which may be one of the reasons of mismatch of stable Saturn rings predicted numerically [Stark 2001] (on particle sizes $< 1 \mu\text{m}$) and those observed experimentally [Gu and Abbott 2000; Mondain-Monval et al. 1999] (on large particles on the order of tens of microns).

Such a discontinuity in the calculation of molecular orientation at singularities (defect cores) was avoided in simulations by Feng and Zhou [2004], which uses a mean-field theory to calculate the stability of defect types. The results are in general agreement with previous suggestions; that the Saturn-ring's stability decreases with increase of particle size although the threshold for absolute stability (global minimum) of Saturn-ring defects differs (being on micrometer scale) from that previously calculated.

Experimental observations are needed to establish a consistent picture on the range of stability of these two defect types in terms of particle sizes and the strength of surface anchoring. One such study involving in-situ variation of bubble sizes was conducted by Voltz et al. [2006], as described below.

1.6.1.2 Experimental

The experimental verification of the theoretically predicted particle-size-induced transition between defects has been hindered by the lack of dynamic size variation of the particles. The experiments by Voltz et al. [2006] aimed to demonstrate this transition in-situ. They used a high pressure technique to vary the size of air bubbles confined in a planarly anchored LC cell. They observed that, as the bubble size is reduced there is a transition from hyperbolic hedgehog defect configuration to Saturn-ring configuration. This transition was predicted to occur between bubble radii of 1 μm to 5 μm .

Experiments by Monval et al. [1999] focussed on the weak surface anchoring on water droplets suspended in host LC medium. They observed primarily, the occurrence of quadrupolar equatorial ring defects for particles on the scale of few tens of microns with occasional occurrences of hedgehog defects also. This suggests that the two defect types can be meta-stable in conditions of weak anchoring. However, they did not mention the range of anchoring energy ratio, Wa/K , applicable to their experiments.

Other experiments [Loudet and Poulin 2001] on colloidal particles (evolving from phase separation mechanism) in liquid crystals, indicate the formation of quadrupolar distortions on droplets with sizes as large as few microns in diameter. These quadrupolar droplets grow in size by coalescence due to elastic quadrupolar attraction, ultimately reaching a critical radius where the quadrupolar ring loses its energetic favourability and transforms into a dipolar hedgehog defect. Although the trend of Saturn-ring structure being preferred for lower W values, is in agreement with previous theoretical calculations, the upper limit on the radius ($\approx 3.75 \mu\text{m}$) of their drops possessing Saturn-rings, is higher than that theoretically predicted [Lubensky et al. 1998; Ruhwandl and Terentjev 1997; Stark 1999].

1.6.2 Effect of External fields

The magnetic susceptibility of liquid crystal molecules is sufficient to induce distortions in the director in the presence of field. When a magnetic field is applied, the molecules experience a net torque, which tends to rotate them parallel or perpendicular to the direction of the applied field depending on whether the diamagnetic susceptibility of the liquid crystal is positive or negative.

The effect of a strong magnetic field is thus, to compress the field lines to create high densities of elastic and magnetic free energies which has an effect on the stability of the defect type.

1.6.2.1 Computational

Stark [1999] and Grollau et al. [2003] have calculated that a magnetic field of sufficient strength will result in Saturn-ring achieving lower energy than a dipole even if the dipole was the preferred configuration in the absence of field. A transition from dipole to ring will occur by the application of magnetic field, and for smaller particles, the Saturn-ring remains meta-stable while the field is turned off.

1.6.2.2 Experimental

Gu and Abbott [2000] investigated the presence of defects on solid particles, treated to impose homeotropic surface anchoring, in an LC cell with planar anchoring. They observed the microspheres (40 μm to 100 μm in diameter in a 120 μm thick cell) to be occupied by stable (some > 1 month) Saturn-ring defects, contrary to previous predictions [Lubensky et al. 1998; Stark 2001]. However, this was later predicted computationally [Grollau et al. 2003; Stark 2002], to be a confinement induced effect, akin to the application of magnetic field. Besides these, they also observed some spheres to be surrounded by defects of a dipolar nature, and suggested that they may have been formed by spontaneous transformation from Saturn-ring defects. However, such transitions were not captured, so the details of their occurrences were not clear. Also, it was not verified whether an isotropic droplet suspended in LC medium and possessing a dipolar state would be converted to a quadrupolar state by the application of field, although their experiments showed the expansion of stable Saturn-rings upon application of electric field.

More convincing experimental evidence was provided later by Loudet & Poulin [2001]. They used phase separated silicone oil droplets suspended in bulk LC phase. In equilibrium and absence of field, these droplets possessed a dipolar point defect. Upon application of electric field it opened up into a quadrupolar equatorial ring defect. Further, the threshold field for this conversion depended on the strength surface anchoring (Wa). As the droplet size increased, the tendency to achieve dipolar state also increased, and thus due to a higher activation energy, the droplets required a higher threshold field to induce this transition. The transition was found to occur in a span of less than 1 second and was believed to be because of instability of hyperbolic

hedgehog rather than thermodynamically driven transition between metastable states. Upon cessation of field, the dipolar state always returned, with relaxation time of the order of few tens of seconds. So under their experimental conditions the metastability of the two configurations was either weak or absent.

1.6.3 Effect of flow

The effect of a flow field on the defects has received far less attention. Flow of nematics is more interesting and complex than classical isotropic fluids due to the coupling of director field and velocity. Motion and flow are involved in various dynamic processes in nematic dispersions, e.g. the self-assembly of micro-droplets [Poulin and Weitz 1998], and a thorough understanding of the hydrodynamic effects on defect evolution will be valuable.

1.6.3.1 Contradictory Computational predictions

So far, there have been several computational studies. Stark and Ventzki [2002] predicted that, flow around a particle will move a satellite point defect against the direction of flow for finite Ericksen numbers Er , defined as the ratio of viscous to elastic forces: $Er = \eta av/K$, where η is the viscosity of the medium, a and v are the particle radius and velocity, and K is the bulk elastic constant. This counter-intuitive motion of defect was attributed to a minimized resistance to flow. It was also postulated that, for large Er , the satellite point defect would open up to form a more stable Saturn-ring defect, which can then move upstream.

This prediction was later contradicted by Yoneya et al. [2005] whose calculations predicted that an initial satellite point defect near a particle is stable under flow, and that its motion would be along the direction of flow. For flow direction from particle to defect, the defect would get convected far in the wake and would not transform to a Saturn-ring defect. An initial Saturn-ring was predicted to be continuously swept in the flow direction, and ultimately converge to a stable hedgehog point defect in the wake. More recently, simulations by Zhou et al. [2007] suggested that a defect ring around a rising drop convects downstream as the rise velocity increases, and may be transformed into a point defect in the wake.

Since the defect is not a physical entity, its apparent ‘convection’ reflects rearrangement of the orientational field rather than flow of materials. Thus, it is not intuitively obvious which

prediction is correct. Furthermore, the intricate details of nematodynamics, involving the coupling of molecular anisotropy with hydrodynamics of flow, make it difficult to unravel the contradictory predictions.

1.7 Objective and Scope of this thesis

This work involves the experimental study of defect dynamics around drops and bubbles rising in a nematic liquid crystal. It aims to resolve the contradictions in literature regarding the behaviour of a hyperbolic point defect and a Saturn-ring defect under hydrodynamic flow. In particular, we seek a clear picture of the stability and the direction of motion of a hyperbolic point defect with respect to the flow direction and whether flow can induce a structural transition of either defect type.

We present direct experimental evidence for the downstream convection of a point defect, and its subsequent retraction in the wake of a rising bubble. Flow induced defect transformation, from Saturn-ring to a point defect, was observed. A surprising spontaneous transition, from satellite point defect to a Saturn-ring defect, on static drops and bubbles was also captured. Quantitative analysis involving measurements of flow velocities and defect locations yields data that is consistent with previous theoretical calculations.

2 EXPERIMENTAL MATERIALS AND METHODS

This chapter describes the working principles that are involved in the experimental observation and which are necessary for the understanding of the results. It also provides the details on the experimental setup and the methods used.

2.1 *Observation of Liquid Crystals*

Owing to their optical anisotropy, liquid crystals have traditionally been observed with the help of polarized light microscopy. Samples of liquid crystals sandwiched between glass slides, yield regions of a good contrast (due to the varying orientation of optic axis). In addition, because of their turbidity due to light scattering by director fluctuations [Durand et al. 1969], care has to be taken to make the nematic sample thickness to ‘sub-millimetre’ scale, lest the optical clarity and uniformity of anchoring be sacrificed.

Due to the dynamic nature of our experiments, we have customized an experimental system for the purpose of flow observation of moving bubbles and droplets. This involves the use of a polarizing microscope and an accurately (with speed precision of few $\mu\text{m/s}$) controlled motion-control system coupled to the microscope. The experimental runs are conducted in a fabricated micro-flow-cell. An experimental protocol for this fabrication process has been established and benchmarked, following which we conduct the desired runs. We also incorporate the relatively new technique of measuring retardances and molecular orientation using a quantitative imaging system, first developed by Oldenbourg [Guang and Oldenbourg 1994; Oldenbourg and Mei 1995] and later commercialized by CRI Inc as Abrio™. We have used it to determine the director orientation in a nematic liquid crystal and around bubbles and drops submerged in the nematic medium.

2.2 *Polarized light*

Light, because of its electromagnetic nature, is subject to polarization. Polarization of light describes the direction of oscillation of electric or magnetic field in a plane perpendicular to the direction of travel. Mathematically, the amplitude of electric field for a light wave polarized in x direction and travelling in the z direction can be described by the wave equation:

$$E(z, t) = E_x^o \sin[2\pi vt - 2\pi z/\lambda + \phi_o] \quad (5)$$

Here,

E_x^o is the maximum amplitude of the light wave, v is the frequency, λ is the wavelength and ϕ_o is a constant specifying its absolute phase.

Thus, in the above instance, light is depicted as being linearly polarized. However, depending on the amplitude (E) and phase difference ($\Delta\phi$), it can also be circularly or elliptically polarized; circular and linear polarization being special cases of elliptical polarization. Typically, to convert unpolarized light to polarized light, optical materials known as polarizers are used.

2.2.1 Light Propagation through a liquid crystalline medium

Birefringence or double refraction, is the decomposition of a light ray into two rays - the ordinary ray (o-ray) and the extraordinary ray (e-ray), when it passes through an anisotropic medium. It is manifested as a result of orientation-dependent differences in the refractive index of a material. The o-wave behaves as in travelling in an isotropic medium, but for the e-wave, the refractive index depends on the direction of propagation. Due to the anisotropic nature of liquid crystal molecules, this property of birefringence can easily be tapped to study their orientation under polarized light. Mathematically,

$$\text{Birefringence} = |n_e - n_o| \quad (6)$$

Here, n_e and n_o are the refractive indices experienced by the extraordinary and ordinary rays, respectively.

A related term, the retardance (optical path difference) is defined by the relative phase shift between the ordinary and extraordinary rays, as they emerge from the anisotropic material. In general, for a material having uniform refractive indices n_1 and n_2 and thickness t :

$$\text{Retardance, } \Delta\Phi = (n_1 - n_2) \cdot t \quad (7)$$

In other words, Retardance = Birefringence times the Thickness of the birefringent medium

For calamitic liquid crystals (e.g. 5CB), the plane of polarization of the e-wave always contains the director \mathbf{n} , whereas the o-wave is always polarized normally to \mathbf{n} . Consider a nematic medium confined between two glass plates and placed between crossed polarizers. Let the director \mathbf{n} be in the plane of the plates. Unpolarized light upon passing through the first polarizer becomes linearly polarized with intensity $I_0 = E^2$, where E is the amplitude of the wave. When this wave passes through the nematic sample, it splits into two mutually perpendicular ordinary and extraordinary waves. As discussed before due to the different refractive indices experienced by these waves as they exit they emerge with a net phase difference, $\Delta\Phi = 2\pi d (n_e - n_o) / \lambda_0$, where λ_0 is the wavelength of light in vacuum.

The second polarizer (also called the analyzer) with optic axis perpendicular to the first one (crossed state), transforms this phase difference into the pattern of transmitted light intensity, thus eventually yielding [Kleman and Lavrentovich 2003]:

$$I = I_0 \sin^2 2\beta \sin^2 \left[\frac{\pi d}{\lambda_0} (n_e - n_o) \right], \quad (8)$$

with the condition that \mathbf{n} is perpendicular to z -axis, and β is the angle between local \mathbf{n} and polarization direction of incident light.

However, if \mathbf{n} makes a constant angle θ with z -axis, the transmitted intensity would be:

$$I = I_0 \sin^2 2\beta \sin^2 \left[\pi \frac{d}{\lambda_0} \left(\frac{n_o n_e}{\sqrt{n_e^2 \cos^2 \theta + n_o^2 \sin^2 \theta}} - n_o \right) \right] \quad (9)$$

Thus, wherever \mathbf{n} is parallel to either polarizer the propagating wave is either purely ordinary or purely extraordinary, and the corresponding region in the sample would appear dark. Similarly, \mathbf{n} making an angle of 45° with the polarizer axis would result in regions of maximum intensity.

2.3 Quantitative Imaging using Abrio

The use of a quantitative imaging system is made for the measurement of liquid crystal director in the region of interest. The imaging system is akin to using a rotating polarizer, with the advantage that it eliminates the 90° orientation ambiguity present when viewing through crossed

polarizers. It uses a liquid crystal compensator device and special image processing algorithms to measure optical polarization parameters at many points simultaneously, in fast time intervals, thus generating a birefringence map from measured intensities. This map depicts the retardance and slow axis orientation at the pixel level.

Abrio has been used previously to successfully measure details of living cells, viz. the spindles in dividing cells, monitor vesicle trafficking, observe cell-to-cell interactions, and monitor cytoskeletal reconstruction [Katoh et al. 1997; Oldenbourg 1999; Oldenbourg et al. 1998]. An application of Abrio to observe liquid crystalline state appeared recently [Wu and Mather 2005] where Abrio was used successfully to map the orientation of liquid crystalline polymer near the nematic isotropic interface.

The elementary components of the system include: a CCD digital camera, a liquid-crystal (LC) compensator optic, a circular polarizer/interference filter optic (CP/IF) and an image processing software (see appendix for layout). The CCD camera is connected to the LC compensator and is interfaced with the computer via USB. The compensator fits into the analyzer position in the microscope. The circular polarizer creates monochromatic circularly polarized light, while the LC compensator changes the polarization states according to commands from the software. Note that for the operation of Abrio's quantitative imaging module, other optical elements like the linear polarizers, have to be disengaged completely from the light path and the LC compensator should be inserted in place of the analyzer. The liquid crystal we use (see section 2.11) is positively uniaxial [Cognard 1982], hence the actual director orientation is parallel to the slow axis direction calculated by Abrio. With the highest magnification objective of 40x, retardances at a pixel level of 0.25 μm can be measured, and the orientation vector's length is averaged over 8 such pixels (2 μm). Abrio's other specifications can be found at the appendix. As a reference standard for Abrio's prediction capability on the setup we conducted a series of benchmarks, some of which are mentioned later in this chapter.

2.3.1 Restriction imposed by Abrio

A limitation of Abrio for samples which produce retardation greater than half the wavelength of light used ($\lambda/2 = 273 \text{ nm}$) is that it depicts the calculated slow-axis director in a manner which is turned by 90 degrees with respect to the true orientation, for sample retardance values lying

between every $m\lambda/2$ and $(m+1)\lambda/2$, where $m = 1, 3, 5, \dots$. According to Oldenbourg [Goldman and Spector 2005], the expressions Abrio uses for calculating retardance and azimuth are:

Retardance,

$$R = \arctan \left[\sqrt{A^2 + B^2} \right] \quad \text{if } I_2 + I_3 - 2I_1 \geq 0 \text{ and}$$

$$R = 180^\circ - \arctan \left[\sqrt{A^2 + B^2} \right] \quad \text{if } I_2 + I_3 - 2I_1 < 0 \quad (10)$$

Azimuth,

$$\Phi = \frac{1}{2} \arctan \left(\frac{A}{B} \right) \quad (11)$$

Here, I_1 , I_2 , I_3 and I_4 are the measured instantaneous image intensity values for different compensator settings and A and B are the intermediate results based on image intensities. However, if the actual retardance is in the range $\lambda/2 < R_0 < \lambda$, the measured retardance is: $R = \lambda - R_0$ and azimuth is turned by 90° , and if $\lambda < R_0 < 3\lambda/2$ then $R = R_0 - \lambda$ and the azimuth will be measured correctly.

Taking the birefringence of liquid crystal 5CB ≈ 0.17 (see appendix for reference), we find that this retardance-limit overshoot will occur for samples having thickness $d \approx > 1.8 \mu\text{m}$, which is always the case. However, this ‘retardance–turning’ phenomenon (which leads to incorrectly measured orientations) is not a serious hindrance because its presence can be located by studying the retardance jumps and falls in moving across the sample region. An example of such a procedure will be given in subsection 2.6 for a wedged cell. Hence, by knowing the wall anchoring direction (as prepared), one can determine regions of correct and turned orientations; the latter can then be corrected by turning the incorrect orientations by 90 degrees.

2.4 Schlieren Texture

To check the accuracy of Abrio in measuring the liquid crystal director orientation, we imaged samples containing defects with known orientations. The following is one such example of the Schlieren texture often observed in liquid crystals [Chandrasekhar 1992; de Gennes and Prost 1993].

If the boundary conditions confining a liquid crystal sample are degenerate, there would typically exist a system of point like discontinuities which, when observed through crossed polarizers, appear to be connected by black bands. The resulting texture is called a Schlieren texture. The dark bands (or brushes) arise in regions where the optical axis of the material is either parallel or perpendicular to the plane of polarization of incident light. This causes zero light transmission through the second polarizer. Figure 6 shows the comparison between a crossed polarizers' image and Abrio's orientation vector image which clearly elicits the correspondence in director pattern leading to a defect of strength +1 around the defect core. The Abrio image comprises of coloured regions depicting orientation vector at different azimuth (differentiated by colour), and the contrast indicates the retardance suffered by the sample, retardance being higher for brighter regions. For easy director identification, the orientation vector map is superimposed on the image.

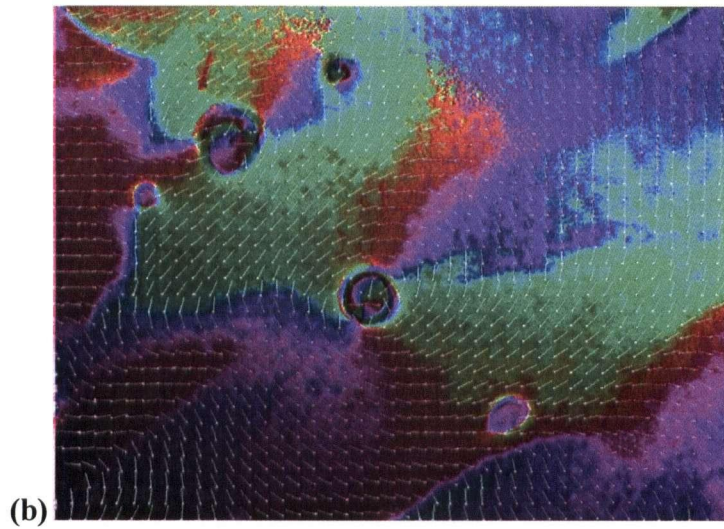
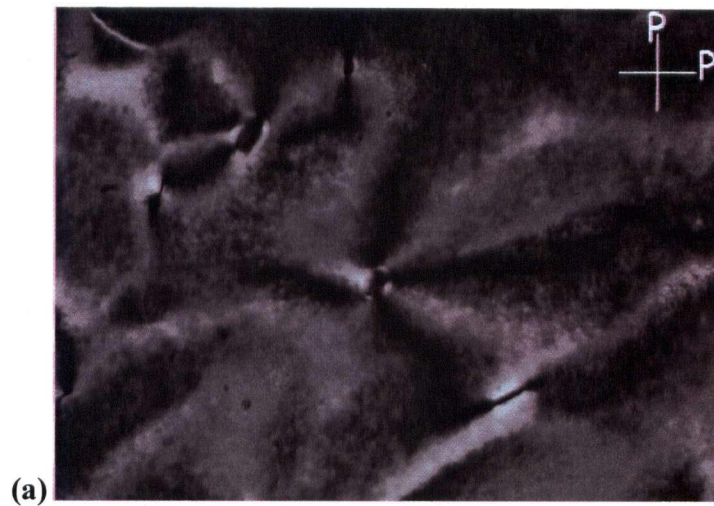


Figure 6: Schlieren pattern in a thin sample of liquid crystal (no wall anchoring) as seen through crossed polarizers (a) , and the corresponding Abrio snapshot (b) with the superimposed orientation vectors.

2.5 Cell fabrication and preparation

The cell preparation can be broadly classified into 3 steps:

- (1) Decontamination of substrate
- (2) Polymer deposition and rubbing
- (3) Sealing and filling

(1) Decontamination of substrate:

Standard pre-cleaned glass slides (75 mm x 50 mm) were initially rinsed with distilled water to remove visible particulate contaminants. These were then put in a concentrated cleaning solution (Micro-90, Sigma-Aldrich) using distilled water and heated for > 20 minutes. These were then, rinsed again with distilled water followed by a thorough rinsing with de-ionized filtered water. Finally, they were blow dried in a stream of hot air. Immediately before the deposition process, they were impinged with a blast of pressurised air for removal of any residual particulates.

(2) Polymer deposition and rubbing:

Planar wall anchoring was achieved using the process of mechanical rubbing of a layer of polymer deposited on the substrate. The polymer chosen was Poly-Vinyl Alcohol (PVA) (> 99% purity, Sigma-Aldrich). A solution of 3 - 4 % PVA was prepared in deionised water by simultaneous mixing and heating. This was allowed to cool to room temperature. The cleaned slides were dipped into the beaker containing the prepared solution, thus resulting in deposition of a thin layer of solution, the uniformity of which was confirmed by looking obliquely under bright light. The slides were then placed to dry for at least 30 min at 100 °C in a preheated oven. After letting cool to room temperature, these were rubbed unidirectionally many times with a lens cleaning tissue. This unidirectional rubbing stretches the polymer chains along the direction of rubbing which then helps promote planar anchoring of LC molecules [Cognard 1982].

(3) Sealing and filling:

For achieving a uniform gap, polyester spacers, having thicknesses in the range of 100 to 500 microns, were used. These were cut to the desired size and cleaned in a similar manner as the slides. The prepared slides were sandwiched together with the spacers in between, and were sealed all along the edges, with a quick curing epoxy, leaving a couple of holes for filling. The cell gap was changed asymmetrically (by using spacers of different thickness) for making a wedged cell, wherein the distance between the cell walls varied along the plane of the wall. Whenever required, a clean micro-capillary was carefully placed inside the cell near one of the edges before sealing. The cell was allowed to cure overnight. Once ready, it was filled with the LC using a cleaned Pasteur pipette. Figure 7 shows an illustration of how the components are layered in the fabricated cell.

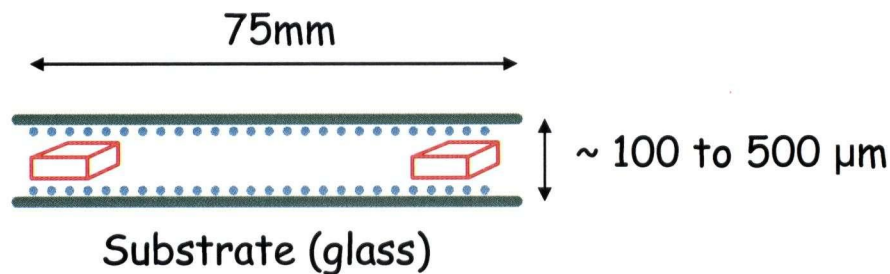


Figure 7: Schematic of a fabricated cell

2.6 Uniform Planar Wall Anchoring

We have used Abrio to confirm the uniformity of planar anchoring on the walls of the cell. Thus, imaging a cell with varying gap, i.e. where the thickness of filled liquid crystal varies along the plane of the cell-wall (also called a wedged cell, see Figure 8), and having planar wall anchoring should yield orientation vectors in the anchoring direction (which in turn corresponds to the rubbing direction). However, because of a restriction in the operation of Abrio (explained before in section 2.3.1), the actual vector map is not unidirectional throughout, but has prominent periodically striped pattern where the depicted orientation is turned by 90 degrees after each striped layer, as shown in Figure 9. Nevertheless, the extent and direction of uniformity can still be determined unambiguously.

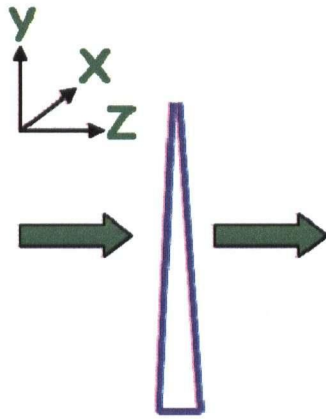


Figure 8: Schematic showing the direction of light path through the plane of observation (X-Y) in a wedged cell.

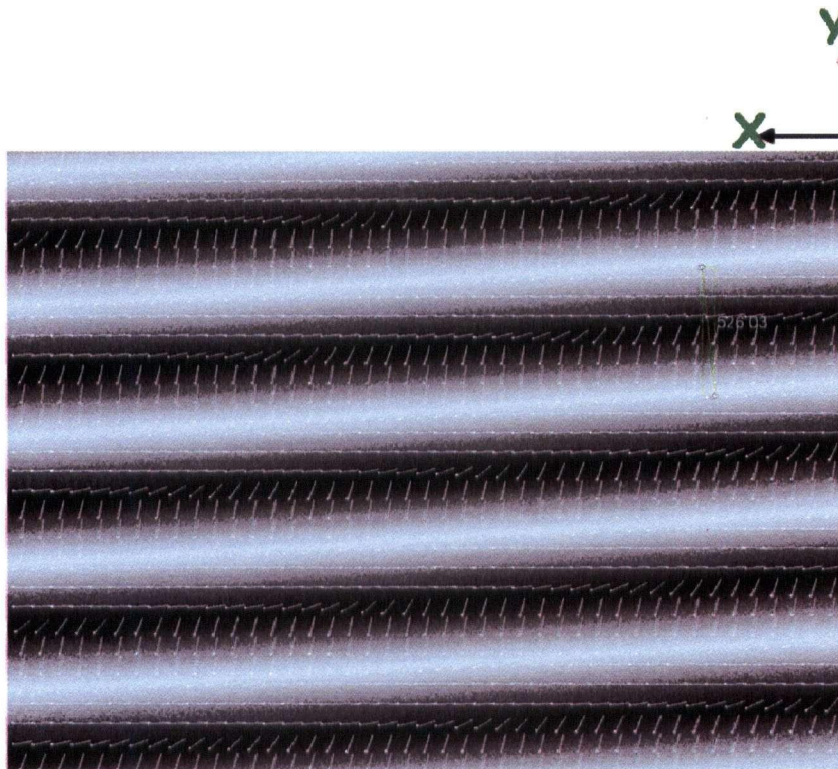


Figure 9: Abrio snapshot of a wedged cell leading to the appearance of retardance bands.

2.7 Anchoring at 5CB-air interface

To check the anchoring direction at the air-liquid crystal interface, a small drop of liquid crystal was placed on a cleaned glass slide. Upon imaging through crossed polarizers, we saw a clear image of a dark cross inside the drop (see Figure 10(a)). This may arise from a radial director pattern inside the drop, where the dark regions correspond to a director parallel to the optic axis of either polarizers. Yet, the mere presence of a dark cross does not confirm a radial director pattern because of the 90 degree ambiguity imposed by the optic axis of the crossed polarizers. For example, a concentric director profile can also lead to such dark crosses. However, this ambiguity can be removed if we image the drop using Abrisio to measure the director orientation and retardance. The calculated director map is found to be radial (see Figure 10(b)) making the analogy with Figure 10(a) apparent.

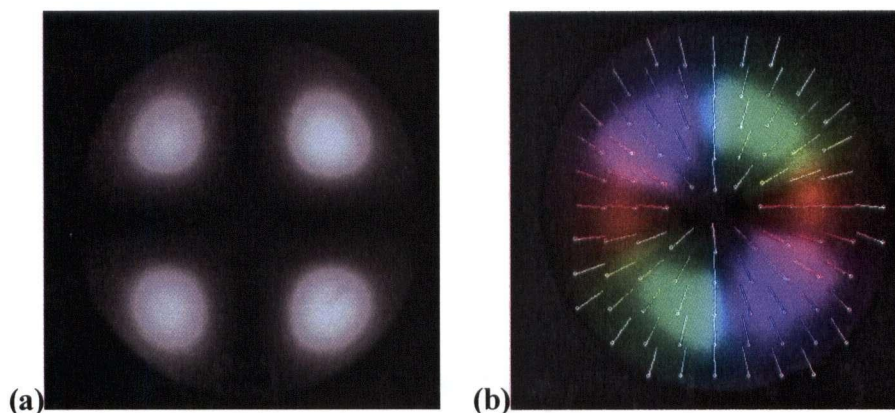


Figure 10: Crossed polarizers image (a) and the corresponding Abrisio snapshot (b) of a thin drop of LC placed on a glass slide.

In another test where a thin film of liquid crystal spread on a glass slide in contact with air, is imaged, we find that the anchoring near 5CB-air interface is again, homeotropic (Figure 11), thus confirming previous tests. This is also in agreement with measurements done by others [Gannon and Faber 1978; Kasten and Strobl 1995].

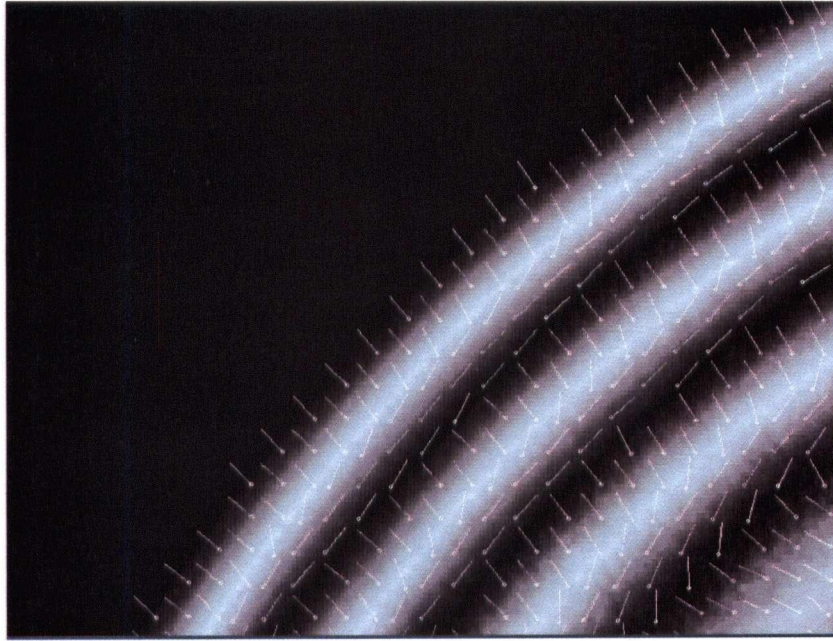


Figure 11: Abrio snapshot of a 5CB film sitting on a single glass slide exposed to air. The intensity indicates the measured retardance and the superimposed vectors represent the LC-director. Note that the abrupt and repetitive 90 degree turns in the vectors is due to a restriction in Abrio's working and is to be correctly interpreted by rotating through 90 degrees, as mentioned before. The anchoring near air-LC interface is homeotropic.

2.8 Motion Control System and microscope

For continuous and instantaneous observations we tailored* a staged translational motion control system capable of moving along two axes. It consists of a stepper motor coupled to a translational stage (LT1, Thorlabs) capable of uniaxial translation up to 50 mm. Another stage is mounted perpendicular to this and is controlled manually along the x -axis. This system in turn, sits on an aluminium frame which can be mounted to the optical table (see layout in Figure 12). The hardware is connected to the computer with an interface through a Matlab program[†]. The linear speed of the motor, determined experimentally, varies in the range 2 $\mu\text{m/s}$ to 5 mm/s. For air bubbles with velocities up to few tens of $\mu\text{m/s}$, this is good enough to capture an image in real time without producing motion blur. However, for oil drops with rise velocities lower than the lower bound of the motion control, we chose to use the motion control only to occasionally

* Assembly done by CBVL, Vancouver.

[†] Modification done on borrowed version (from Dr. Teodor Burghilea, UBC)

reposition the drop in the field of view. Hence, most of the snapshots for oil drops were taken with a static reference frame.

For observing rising bubbles or drops, we set up the optical microscope in horizontal position rather than the conventional vertical position, as can be seen from Figure 13. The microscope used was an inverted polarizing microscope (Olympus IX-51) fitted with removable crossed polarizers and a set of 4 objective lenses (4x, 10x, 20x, 40x). With these lenses a resolution range of $2.75\ \mu\text{m}$ to $0.42\ \mu\text{m}$ and field of view* of $1410\ \mu\text{m} \times 1140\ \mu\text{m}$ (using 4x objective) to $140\ \mu\text{m} \times 114\ \mu\text{m}$ (using 40x objective) can be achieved. For polarized microscopy, a pair of crossed linear polarizers was introduced in the light path and observations were made under brightfield conditions. These were removed when using Abrio, which requires its own set of optics (compensator and filter) to be inserted. For both polarized and quantitative imaging, images were captured using the attached Abrio ccd-camera.

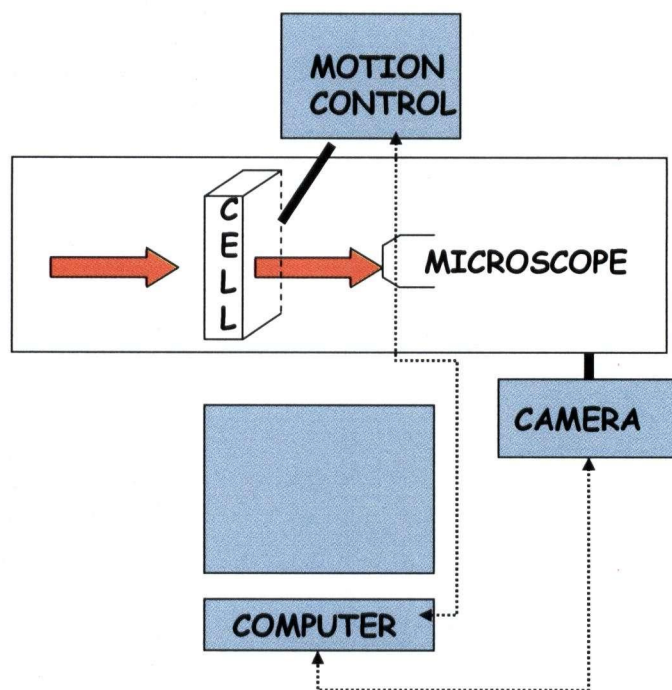


Figure 12: Schematic of the experimental setup

* As measured through the imaging software's window.

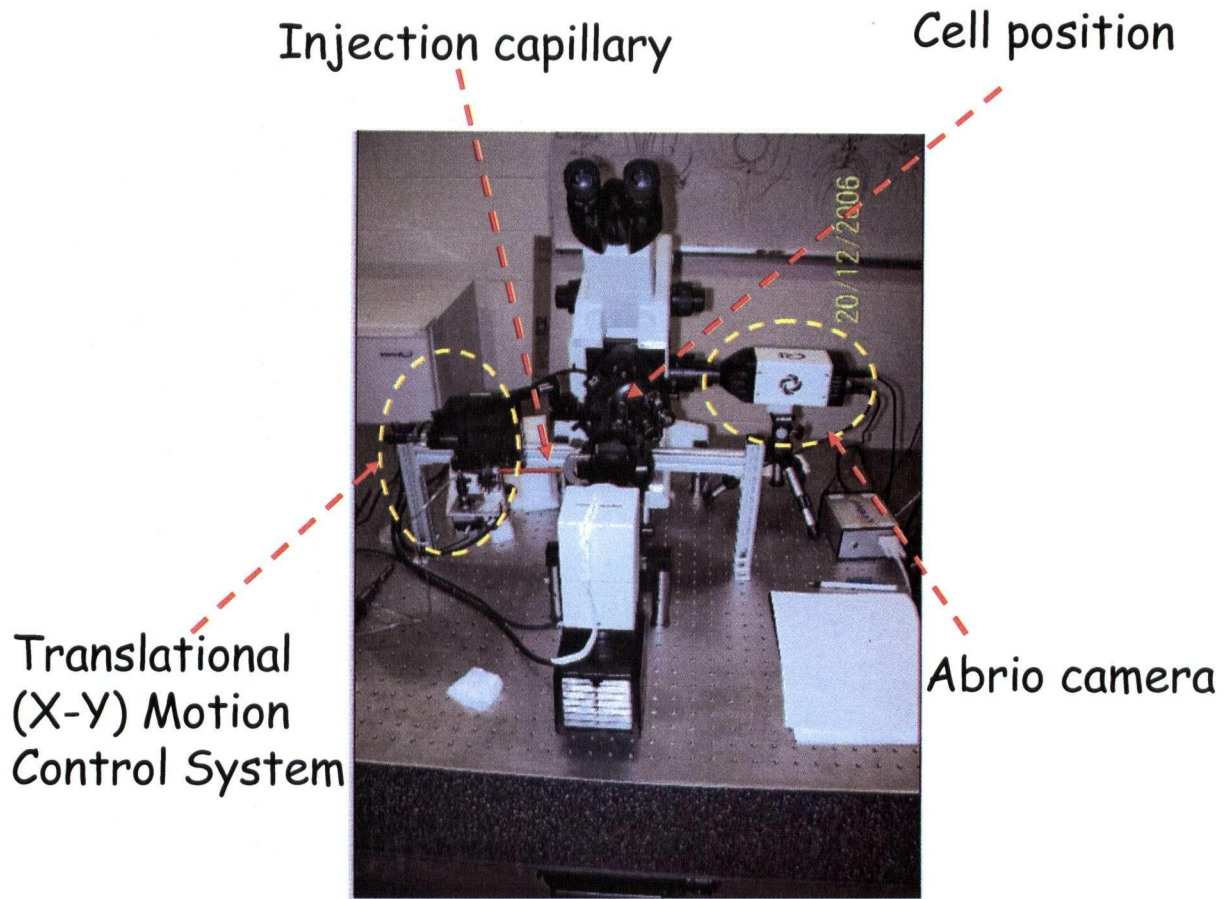


Figure 13: A photograph showing the experimental setup

2.9 *Micro-bubble and micro-drop production*

Consistent and controlled production of micro-bubbles or droplets has always been a challenging task. One of the main reasons is the cube-root dependence of bubble radius on the size of the needle. Assuming a spherical bubble, a balance between surface tension and buoyancy yields:

$$R_c = \left(\frac{3 \sigma r}{2 \rho g} \right)^{\frac{1}{3}} \quad (12)$$

Here, σ is the surface tension coefficient, ρ is the density difference between the bubble and the surrounding fluid, r is the radius of the needle tip, g is the gravitational acceleration and R_c is the critical radius of the bubble or drop

Hence even if r is reduced by a 1000 times, the bubble radius will only decrease one tenth. With air as bubble phase and taking $\sigma = 50 \times 10^{-3} \text{ N/m}$; $\rho = 10^3 \text{ kg/m}^3$; $g = 10 \text{ m/s}^2$; $r = 10^{-4} \text{ m}$ (i.e. $100 \mu\text{m}$) we get, $R_c = 750 \mu\text{m}$.

Several experimental trials with various needles and tips resulted in a minimum attainable radii of few hundreds of microns, still higher than the desirable figure ($< 150 \mu\text{m}$). Other techniques of micro-drop production including piezoelectric nozzle and microfluidic devices seemed difficult to incorporate in the present study. Eventually, a pressure injection technique incorporating a pico-pump was found to be an effective solution. The pneumatic picopump uses carefully regulated positive air pressures for injecting picoliters to millilitres of fluid into a sample. Timing, ejection pressure, and holding pressure can be adjusted independently by control knobs and indicator gauges. Time intervals can range from 10 seconds to 10 ms or less, depending on the ejection pressure which can range from 0.3 to 90 psi. The picopump was used in conjunction with a micro-capillary which was inserted into the fabricated micro-fluidic cell. The air bubbles produced using this technique ranged approximately from 25 to $150 \mu\text{m}$ in radius.

For oil drops, owing to a very small density difference, this method produced rather large drops. Instead, an emulsion based method was useful for providing small drop sizes. The oil was filtered and a small quantity (few drops) was injected into bulk LC in a vial. This was followed by moderate shaking and the resulting emulsion was immediately transferred to the pre-fabricated cell. It must be noted here that the droplet size ranges achieved, critically depended on the ratio of oil phase to LC phase and the intensity and duration of shaking.

2.10 Rising bubble in homeotropically wall anchored cell

To standardize the experimental protocol a series of runs were performed with bubbles rising in a cell in which the wall anchoring was homeotropic. The homeotropic wall anchoring was achieved by depositing a layer of lecithin on the surfaces of the slides as follows:

A few drops of lecithin (dissolved in Chloroform, Sigma-Aldrich) was placed on a cleaned slide, and before much chloroform could evaporate, another slide was immediately placed on top of the first one thus squeezing and spreading the solution in between. Thereafter, the slides were separated by lateral translation resulting in the evaporation of the thin layer of deposited solution.

These were then dried in the oven and sealed together with spacers as described before in the materials and methods section. The finished cell was then placed into the microscope setup for the experimental run.

Ideally, for a perfectly homeotropically anchored LC sample the director would be parallel to the direction of the incident light waves (z-axis). Recalling the relationship between transmitted intensity and the angle (equation 8, section 2.2.1) this will result in zero transmission [Sakagami et al. 1973]. However, under real circumstances (especially in the absence of strong anchoring agents like electric field) there will always occur some deviation from this ideality. Hence, among all the cells tested, there is always the presence of a light background texture. The nematic liquid crystal (5CB) molecules are known to anchor homeotropically at the air-LC interface. A bubble placed in a uniformly aligned bulk LC medium will induce elastic distortions and the LC will tend to minimize the total energy of the system. For the present case, this implies that the angle between the plane of tipping of the director and plane of incidence of light rays will change from 0° to 90° as we approach the bubble surface from far field, where the distortions are minimum (see Figure 14). Thus, it would result in a retardation gradient in the plane of the cell wall leading to an increase in birefringence as we advance towards the interface. This fact is clearly demonstrated by the use of quantitative imaging. Figure 15 show one such run along with the corresponding retardance plot.

For understanding the images we have to understand the consequences of the limitation in the imaging system (described in section 2.3.1). Firstly, we see numerous light and dark bands surrounding the rising bubble. These occur because of the gradient in retardation, which the Abrio system represents as multiple orders of wavelength overlaps in the measured retardances. In other words, each white band (highest intensity) indicates the maximum measured retardance while each dark band (lowest intensity) is indicative of the minimum measured retardance value. Thus as the retardance changes from near zero in the far field to maximum near the bubble surface, the Abrio predicts it as jumps and falls in the measured retardance values, which can clearly be seen from the retardance vs. distance graph. Secondly, the decreasing gap between each crest and trough is due to the non-linear gradient of retardance in the XY plane. The picture becomes clearer when we plot a false colour map superimposed by the orientation vectors (Figure 15(b)).

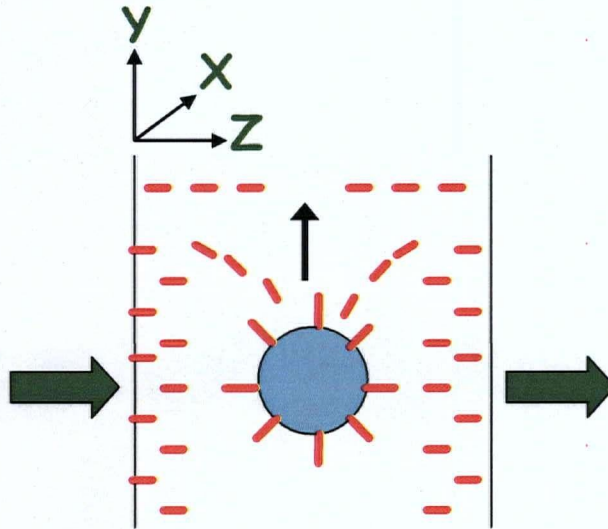
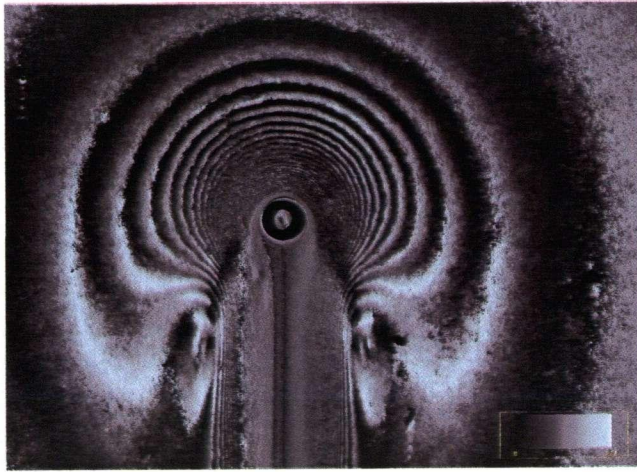
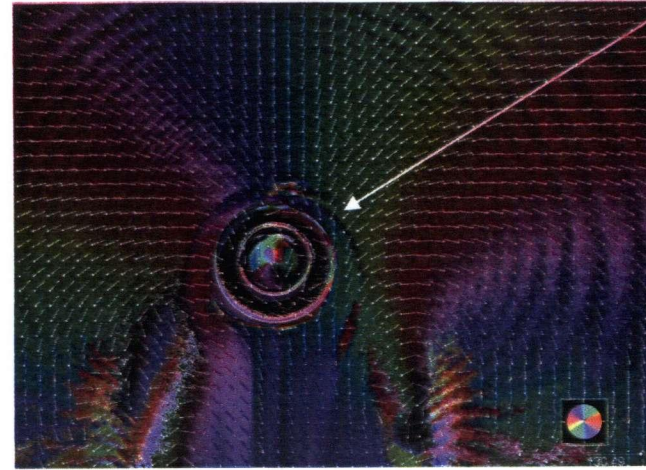


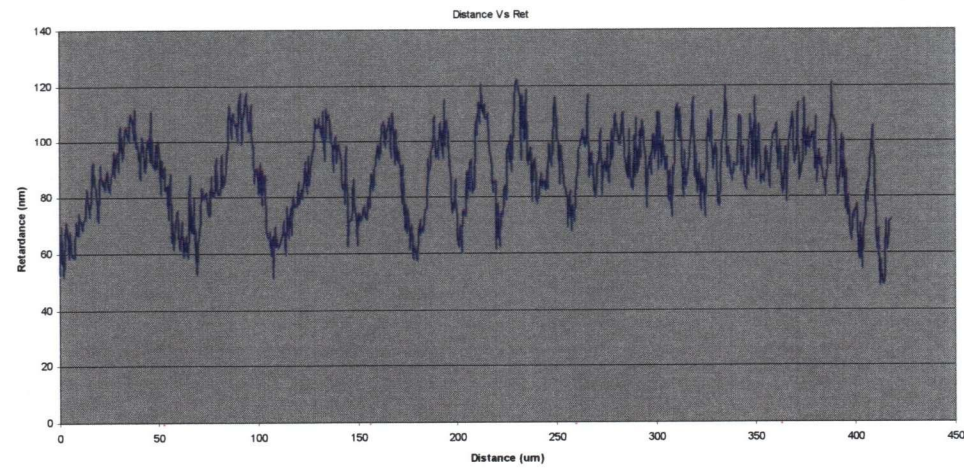
Figure 14: Schematic of a bubble rising in a cell with homeotropic wall anchoring. The anchoring at the bubble surface also being homeotropic, will lead to a relaxed director (shown in red) profile.



(a)



(b)



(c)

Figure 15: A bubble moving in a cell with homeotropic wall anchoring (a) Retardance intensity Abrio snapshot; (b) False colour azimuth profile with superimposed orientation vectors; (c) Retardance vs. distance plot

2.11 Materials used and their properties

The cyanobiphenyl (nCBs) class of liquid crystal compounds are the most studied single-component nematic liquid crystals and are commonly used in liquid crystal displays (LCDs). We use pentyl-cyanobiphenyl (5CB) which is chemically stable over a long period of time (months) and exhibits nematic phase at room temperature. Its properties are well characterised in the literature. The oil used is a light weight viscosity standard silicone oil (polydimethylsiloxane) which yields homeotropic anchoring at the LC-oil interface. Throughout the framework of this thesis, unless otherwise stated, the following material parameters have been used:

Table 1: Material properties

Liquid Crystal 5CB^{††} (98 % Sigma-Aldrich)			
Property	Value	Source/Reference	Comments
Density	$\rho = 1.008$ g/cm ³	Sigma-Aldrich (accompanying MSDS)	
Miesowicz Viscosities	$\eta_1 = 0.051$ Pa-s $\eta_2 = 0.023$ Pa-s $\eta_3 = 0.130$ Pa-s	[Kleman and Lavrentovich 2003]	An effective viscosity, $\eta_{\text{eff}} = 7.65 \times 10^{-2}$ Pa-s is taken for our experimental geometry ^{††} .

^{††} The Liquid crystal was used as such without further purification.

^{††} This value is obtained as an average of the two Miesowicz viscosities with the director along the flow (η_2) and the velocity gradient (η_3) directions, based on the assumption that the third viscosity (η_1) for the 'log-rolling' orientation is irrelevant to our setup

Interfacial tension with Air	$\sigma_{\text{air}} = 35.1$ mN/m	[Tintaru et al. 2001]	Interpolated from graph (T = 24 °C)
Birefringence	$n_e - n_o =$ 0.17	See appendix	$n_e - n_o$ represents the difference in refractive index suffered by e-ray and o-ray
Bulk Elastic Constant	$K = 10^{-11}$ N	[Stark 2002]	This value is widely assumed as the average between the three elastic coefficients of splay, twist and bend.
Anchoring energy constant with Air	$W_{\text{air}} = 10^{-5}$ N/m	[Lavrentovich and Pergamenschchik 1994]	
Anchoring energy constant with Silicone oil	$W_{\text{oil}} = 6 \times 10^{-6}$ N/m	[Lavrentovich et al. 1992]	
Crystal to Nematic to Isotropic (K-N-I) transition temperatures	K – 22 °C – N – 35 °C – I	[Wu et al. 2003]	The values are determined from measurements made in the lab and is in agreement with that in the literature

Silicone Oil ^{§§} (RT5, Cannon Instruments)		
Property	Value	Source/Reference
Density	0.9143 g/mL	From accompanying Report of Calibration
Viscosity	4.690 mPa.s	From accompanying Report of Calibration

^{§§} Reference temperature of 23 °C. The oil was filtered through 0.2 µm filter before use.

3 RESULTS

Defects around isotropic drops in bulk LC medium can be generated with a variety of boundary conditions. For observation axis through the thickness of the fabricated cell, easy identification of these defects requires the use of in-plane wall anchoring. Further, to project the defects to symmetric flow around the vertically rising particle and also to align the director axis with the 'fixed' polarizers' axis, the wall anchoring direction is chosen to be vertical.

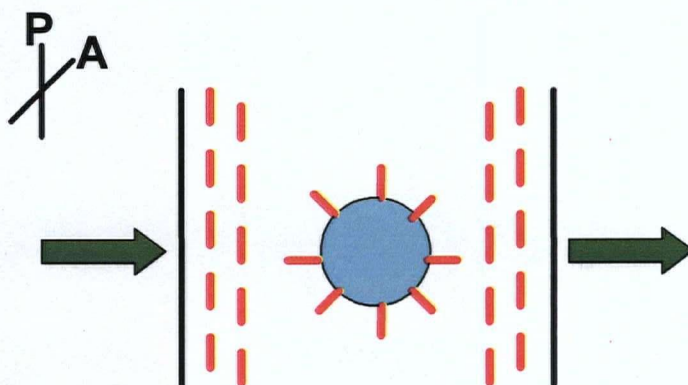


Figure 16: Schematic of a drop/bubble with homeotropic anchoring in a cell with planar wall anchoring. One of the polarizer's optic axis (P) is parallel to the alignment direction and the other polarizer (A) is crossed at 90 degrees to the first one. Light path is indicated by the arrows.

3.1 Defects on static bubbles and droplets

To observe static defects as a baseline, we use a wedge-shaped cell having a thinner gap at the top than the bottom to bring rising drops and bubbles to a stop. Both the Saturn-ring and satellite point defects were observed in equilibrium, each apparently stable as it persists for hours. The ring configuration is apparent in Figure 17(a). Figure 17(b), however, shows two bright lobes separated by a dark line in the middle. Previous observations of defects near droplets imposing homeotropic anchoring [Gu and Abbott 2000; Poulin et al. 1997; Poulin and Weitz 1998] are, to some extent, similar with ours and they have been linked to the presence of a dipolar type defect

near the drop's surface. However, just by comparison, it cannot be made clear whether the observed pattern indeed corresponds to a hyperbolic satellite point defect. We then use computations and quantitative imaging (using Abrio) to help determine the director profile leading to such type of birefringence pattern.

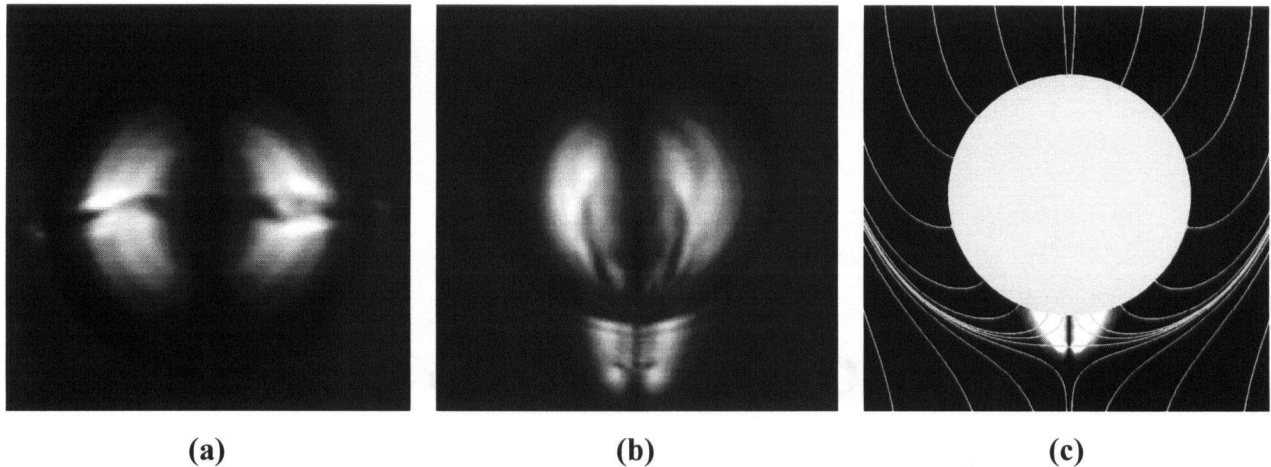


Figure 17: Static defects surrounding oil drops as viewed through crossed polarizers. (a) Saturn-ring defect (drop radius $a = 30.2 \mu\text{m}$); (b) point defect ($a = 21.8 \mu\text{m}$); (c) computed* director field and light intensity graph for a point defect.

3.1.1 Comparison with computed profile

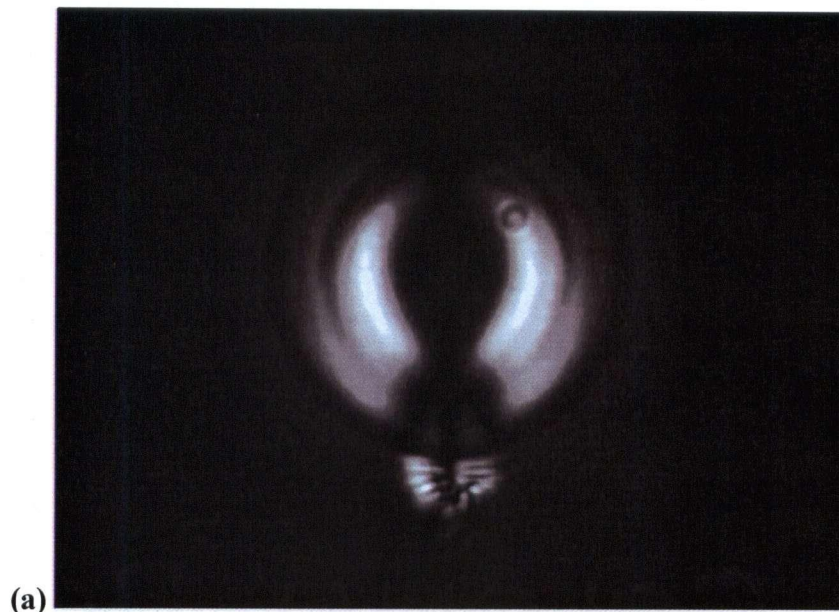
Computations using regularized Frank elasticity [Zhou et al. 2007], help generate an equilibrium director field surrounding a point defect as well as the transmitted light intensity if such a director field is viewed between crossed polarizers. The resulting pattern in Figure 17(c) bears a close resemblance to the observed patterns, with the point defect close to the tip of the bright lobes. This confirms that Figure 17(b) indeed shows a hyperbolic point defect, and the bright lobes are created by director orientation that is roughly midway between the two polarizers.

The stability of the defects depends critically on $A = Wa/K$. For the oil drops in Fig. 1, $a \approx 30 \mu\text{m}$ and $A \approx 18$, for which the two defect configurations are indeed predicted to coexist [Ruhwandl and Terentjev 1997; Zhou et al. 2007]. The distance between the point defect and the center of the drop or bubble, r_d , ranges from $1.14a$ to $1.25a$ among all bubbles and drops tested. The radius of the Saturn ring varies between $1.05a$ and $1.16a$. These are in close agreement with prior computations and observations [Feng and Zhou 2004]

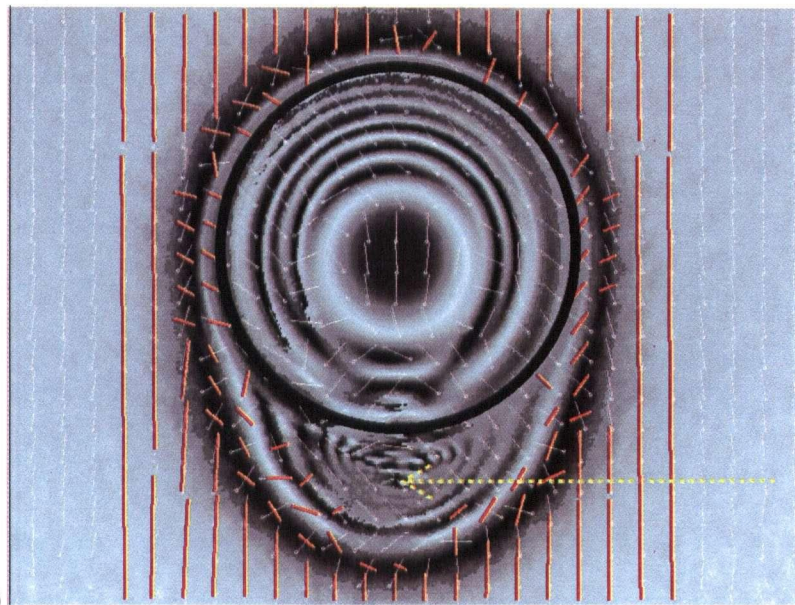
* Computation by Chunfeng Zhou

3.1.2 Comparison with quantitative imaging using Abrio

The use of Abrio's quantitative imaging to measure director orientation of liquid crystals was explained in section 2.10. Figure 18(b) shows the corresponding Abrio snapshot of a droplet with dipolar type defect, seen through crossed polarizers in Figure 18(a). The retardance profile is depicted in greyscale, with retardances ranging from the minimum measurable dark regions ($\rightarrow 0$ nm) to a maximum limit at the brightest regions ($\rightarrow 273$ nm), as we approach the drop surface. If we change the image parameters to depict a superimposed azimuth vector map (red lines in Figure 18 (b)) we can get the related director field. At first glance, the measured director profile does not show the presence of a hyperbolic point defect, though it does indicate an orientation pattern leading to a defect around the drop. Upon more careful visual examination (see greyscale map), the presence of symmetric retardance jumps and falls near the interface (manifested as bright and dark bands in the greyscale image) can be seen. This can be confirmed by plotting a retardance versus distance graph, which yields a sinusoidal wave pattern similar to Figure 15(c), where each crest and trough indicate the upper and lower limits of measurable retardance. As discussed earlier, because of the inability of the system to measure retardances > 273 nm, there occurs a 90 degree twist in the depicted orientation, for each retardance value that lies between $m\lambda/2$ and $(m+1)\lambda/2$; for m being an odd positive integer and $\lambda = 546$ nm is the wavelength of light used. To account for this, we proceed from the known correct far field orientation in the bulk towards the drop interface and artificially turn the depicted orientations in regions lying between alternate retardance bands. Now this does correspond to a profile for a hyperbolic point defect. Again, we must mention here that as we approach the defect core (shown by the arrow), the gradient in retardance increases steeply, as confirmed from the increasing frequency of the sinusoidal retardance plot, thus akin to occurrence of numerous retardance overlaps. This is suggestive of high degree of gradient in the director pattern around the defect, but on the other hand, it also prevents the accurate prediction of actual orientation because the spacing between fringes becomes smaller than individual vector length. Nevertheless, overall the director tends to be homeotropic at the interface and shifts towards bulk planar in far field indicating the presence of a hyperbolic type companion defect.



(a)



(b)

Figure 18: Abrisio snapshot (b) of an oil droplet possessing a dipolar point defect with the corresponding crossed polarizers' image (a). The white vectors represent the measured orientation profile. The red lines are the superimposed edited director orientations, some of which are turned by 90° whenever the retardance falls outside the measurable range (as discussed in section 2.3.1). The LC - drop interface is demarcated by the black circular ring.

3.1.3 Spontaneous and induced point defect to Saturn-ring transition

We observe that occasionally, a point defect spontaneously opened up into a ring that expands and moves towards the bubble's equatorial plane, eventually becoming a Saturn ring (Figure 19). The process of ring expansion was relatively fast, completing within a few minutes (typically < 4). The speed with which the ring opens up was fast in the beginning, but slows down as it progresses towards the equatorial plane indicating the energy cost (instability) it suffers for near polar positions. The point- to-ring transition occurred rather sporadically, sometimes within a few minutes of the stoppage of the drop, sometimes after several hours. This may be a fluctuation-induced transition from one locally stable configuration to the other, suggesting the Saturn ring as the global energy minimiser.

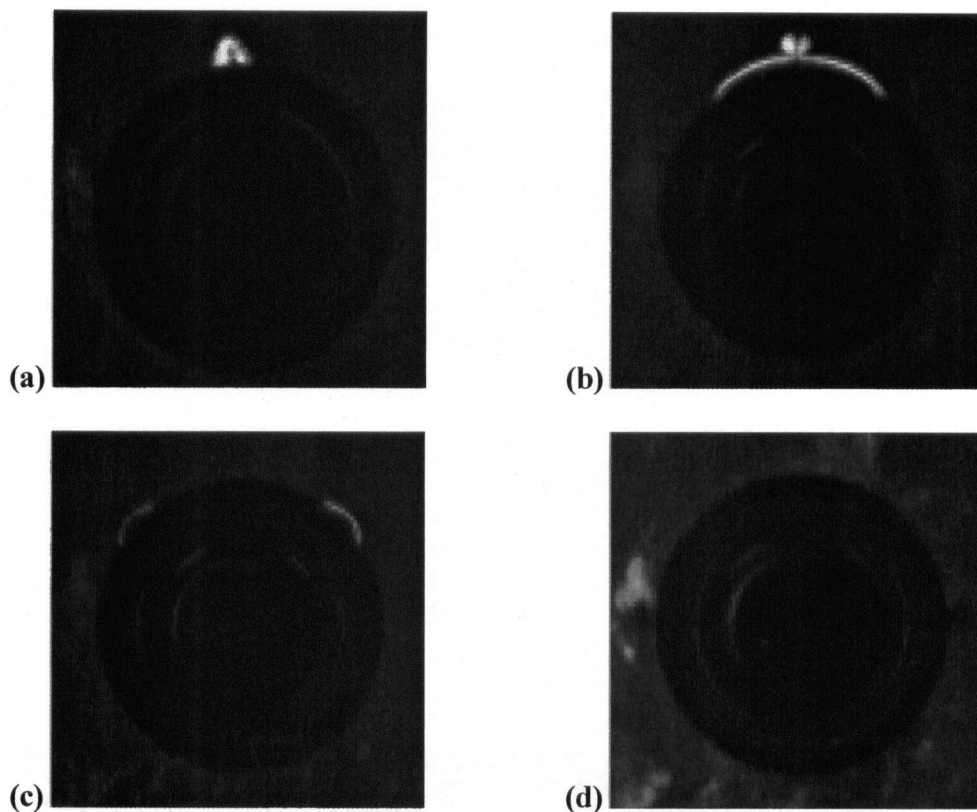


Figure 19: Spontaneous point-to-ring transformation around a stationary bubble of radius $a = 100 \mu\text{m}$. The images were taken through crossed polarizers, and (a) shows the characteristic birefringence pattern for the point defect (cf. Figure 17(c)).

To further probe the stability of the two types of defect, the orientational order was erased momentarily by heating and the system was then allowed to regain its original order. This was

achieved by increasing the temperature of the system to beyond the nematic-isotropic (NI) transition temperature (≈ 35 °C for 5CB) so that the liquid crystal reaches an isotropic state. Allowing it to cool down to room temperature (≈ 24 °C), nucleation of isotropic regions inside the bulk state was observed, which was followed by the formation of Saturn-ring defect. This suggests the ring defect as the globally stable configuration. However, based on the value of A for such incidents, $25 \approx < A < \approx 125$, the point defect is predicted to be globally stable [Ruhwandl and Terentjev 1997; Zhou et al. 2007]. One possible explanation is the effect of wall confinement which was explored by Stark [2002] and later computationally investigated by Grollau and co-workers [Grollau et al. 2003]. Their analysis likens the wall-confinement with application magnetic field which would stabilize the Saturn ring structure. Similar to the effect of

magnetic field (using a magnetic coherence length $\xi_H = \left[\frac{K}{\Delta\chi H^2} \right]^{\frac{1}{2}}$ where, H is the magnetic field and $\Delta\chi$ is the magnetic anisotropy), confining walls would enforce a uniform alignment close to the suspended micro-droplet and scale up the director fluctuations [Mertelj and Copic 2000]. Using the ratio $a/\Delta d$ (where Δd is the distance between particle surface and the wall) as the indicator for the stability of Saturn-ring defect (which occurs when $a/\Delta d \gg 1$), the occurrence of stable Saturn-rings (some stable for over 1 month) on large sized (up to 100 μm in diameter) particles that Gu and Abbott [2000] observed, was accounted for. They also observed what appeared to be spontaneous ring-to-point transformations. Their surface-treated solid particles probably had stronger anchoring that favoured the point defect. In our experimental conditions, even by considering the lower end of particle sizes ($a \approx 30$ μm) and assuming $\Delta d \sim 5$ μm (since the bubbles and drops stop by the effect of wall-confinement) , we find that the ratio $a/\Delta d$ is at least > 6 , and thus much higher than the transition point ~ 1 , hence predicting the stability of Saturn-rings.

Another possibility is that the strength of surface anchoring decreases with temperature increase and may be weak enough near the NI transition temperature so as to skew the ratio Wa/K , encouraging the formation of Saturn-ring defect when the system cools from isotropic to nematic state. Afterwards, the activation energy barrier for transition from one state to another may be high enough to prevent the ring defect from converting back to a point defect, even though the latter might be globally stable. However, based on the current observations (supported by the effect of confinement on Saturn-ring stability) and the fact that in a few instances the dipolar

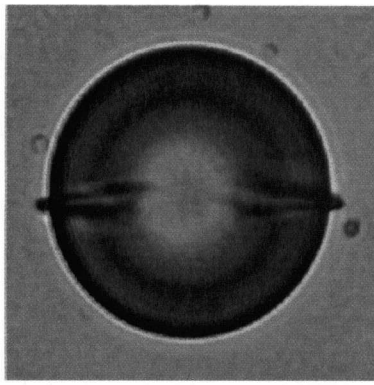
defect opened up to a Saturn-ring even before the system reached the clearing point, we can conclude that for our experimental conditions the Saturn-ring defect is the globally minimum energy state.

3.2 *Oil drops in motion*

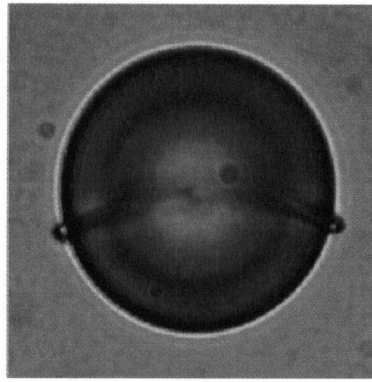
By inverting the wedged cell containing a stationary drop bearing a Saturn ring, we study the evolution of the Saturn ring as the drop rises (Figure 20). During the initial moments of slow creep (rise velocities $v < 0.35 \mu\text{m/s}$), no change in the defect structure is observed (Figure 20(a)). As the rise velocity v increases, the Saturn-ring slowly gets convected downstream (Figure 20(b)). The central part of the ring moves more slowly than the parts near the edge of the drop in the image, thanks to the hindrance by the cell walls. With v approaching the terminal velocity, the ring moves further downstream (Figure 20(d) – (f)) and eventually is swept off the drop into a point defect in the near wake (Figure 20 (g), (h)). For the rest of the drop's rise, the point defect remains stable with no further convection downstream (Figure 20(i)).

This apparent convection of the defects reflects the re-arrangement of the director field $\mathbf{n}(\mathbf{r})$ by viscous and elastic torques [de Gennes and Prost 1993]. Rotation of \mathbf{n} due to the viscous torque (or flow) is on the time scale of the rising bubble, which is on the order of hours (cf. Figure 20). The elastic time scale, on the other hand, is $\eta a^2/K \approx 5 \text{ s}$ for the oil drop with $a = 25.2 \mu\text{m}$. Therefore, except for the fast transient during the shedding of the ring (Figure 20 (f)-(i)), the process is quasi-static as far as the director field is concerned. We then plot the position of the ring or point defect as a function of the instantaneous drop velocity v , non-dimensionalized as the Ericksen number $Er = \eta v a/K$, in Figure 21(a). The initial increase of r_d with Er corresponds to the downstream convection of the ring defect while the drop steadily accelerates. As Er approaches a critical value $Er^c \approx 0.25$, the ring is quickly pushed to the downstream pole with $r_d \rightarrow a$; this is where the ring turns into a point defect. At this moment, the drop velocity drops suddenly (see inset of Figure 21(a)), causing Er to decrease in time and generating the U-turn in the data. Meanwhile, the point defect shifts slowly downstream. Eventually, the drop and defect reach a steady state with $Er \approx 0.19$ and $r_d \approx 1.2a$, indicated by point B. The two outlying circles farthest to the left correspond to the lowest velocity readings in the noisy overshoot. Therefore, for $0.19 \approx Er \approx 0.25$, both the Saturn ring and the point defect are stable solutions.

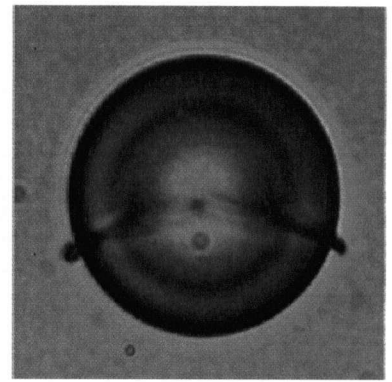
The convection of the ring defect and its transformation into a point defect confirm recent computations of Zhou et al. [2007]. The numerically predicted $r_d(Er)$ curves for steady-state flow are reproduced as Figure 21(b). First, the experimental data follow the qualitative trend predicted numerically, but at lower Er values. The critical value for ring-to-point transformation, $Er^c \approx 0.25$, is below the predicted $Er^c \approx 1$. The discrepancy has several possible origins, including the differing A values, the confinement of the cell walls and various assumptions in the theoretical model [de Gennes and Prost 1993]. Second, Zhou et al. predict the coexistence of the two defect configurations for $Er < Er^c$, which is clearly borne out by the data. For $Er > Er^c$, only the point defect is stable. The oil drops cannot access higher Er and that branch of the numerical curve will be discussed below. Note also that the fast transient in Figure 20 (f) – (h) suggests that these intermediate configurations are not stable steady solutions, in accordance with the jump in the numerical curve of Figure 21(b). Finally, the overshoot of the drop velocity during the ring-to-point transformation has also been predicted, and Zhou et al. rationalized it by the anisotropic viscosity. Overall, the agreement between experiment and simulation is rather astonishing, given that the simulation is based on the simple Leslie-Ericksen theory and contains various simplifications.



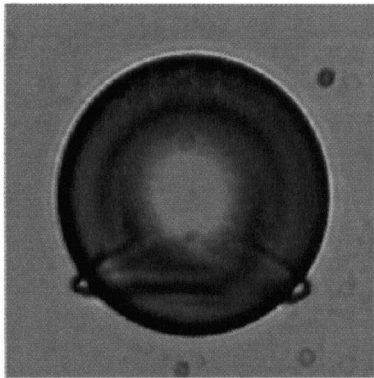
(a) 1074 s, 0.35 $\mu\text{m/s}$



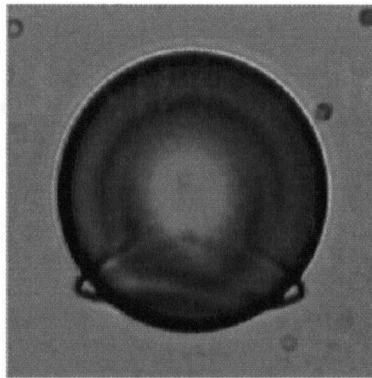
(b) 9323 s, 0.87 $\mu\text{m/s}$



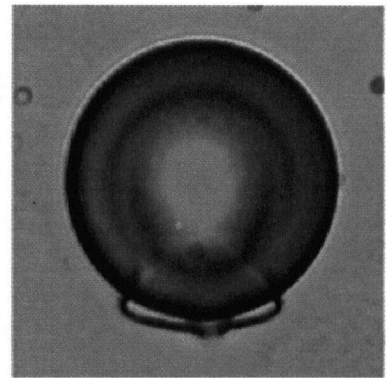
(c) 10542 s, 0.97 $\mu\text{m/s}$



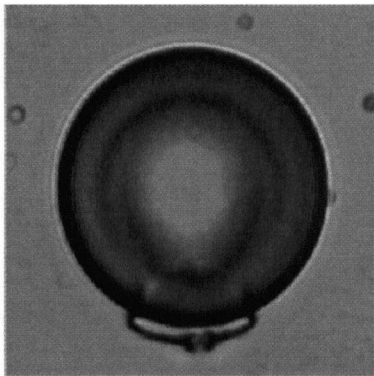
(d) 11425 s, 1.05 $\mu\text{m/s}$



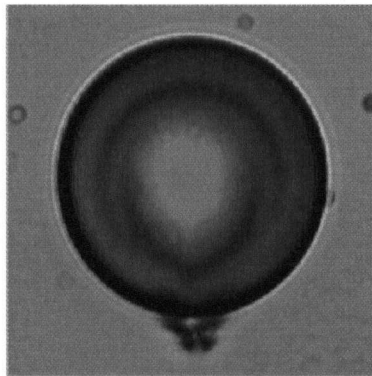
(e) 11430 s, 1.13 $\mu\text{m/s}$



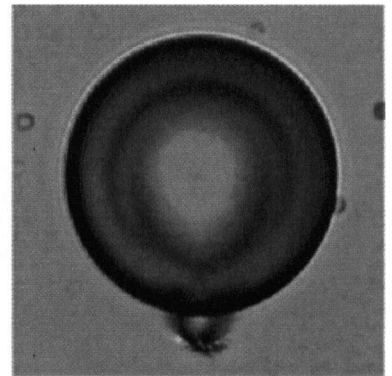
(f) 11444 s, 1.27 $\mu\text{m/s}$



(g) 11445 s, 1.29 $\mu\text{m/s}$



(h) 11447 s, 1.27 $\mu\text{m/s}$



(i) 11448 s, 1.08 $\mu\text{m/s}$

Figure 20: Time series of snapshots showing convection of a Saturn-ring defect (present around a rising oil droplet) and its ultimate convergence to a steady state point defect. The images were taken with single polarizer for clarity.

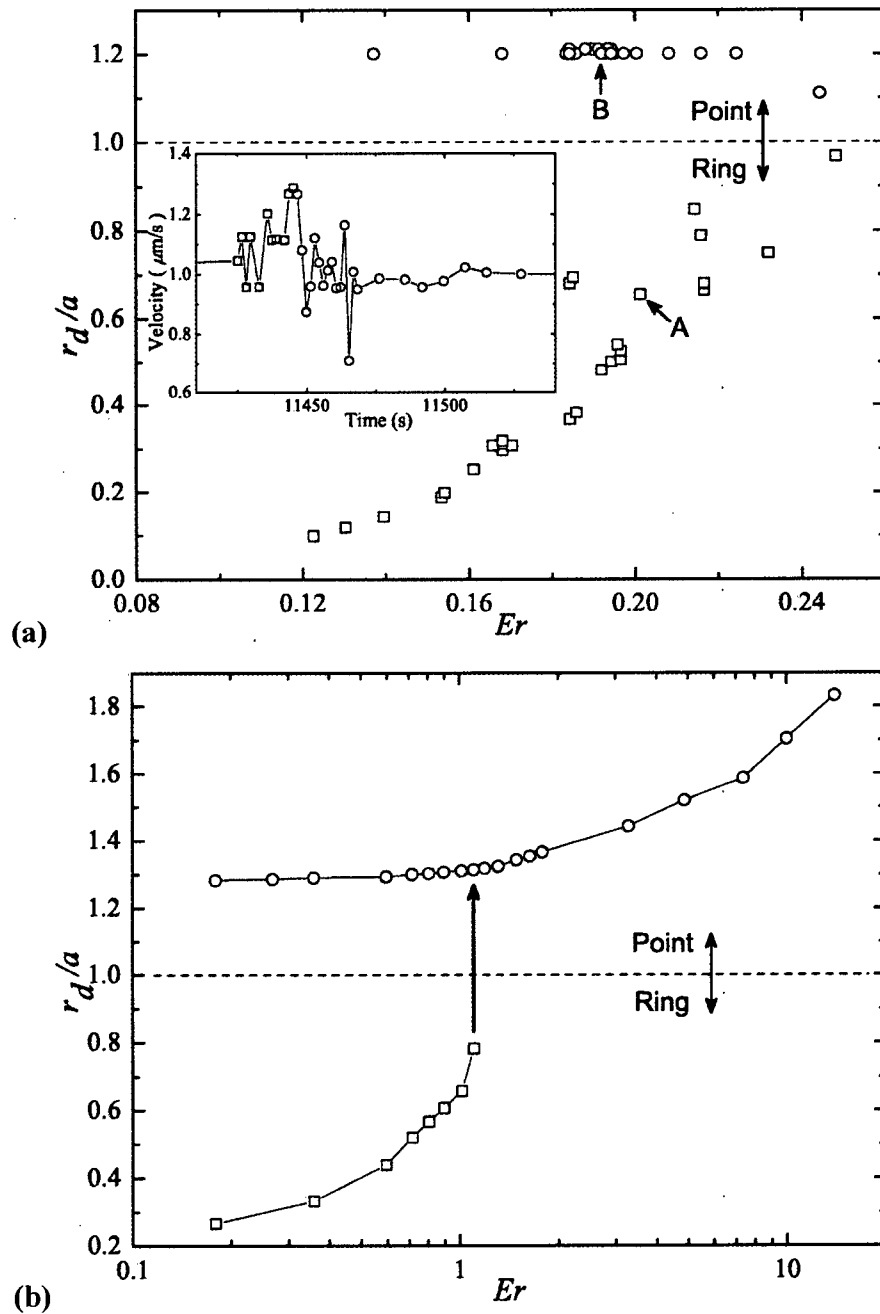


Figure 21: (a) Position of the ring or point defect as a function of Ericksen number ($Er = \eta\nu a/K$) oil droplet run of Figure 20. For the Saturn ring (squares), r_d is the vertical distance between the drop center and the edge of the ring. For the satellite point defect (circles), r_d is the distance from the drop center. $A = 15.1$. The inset shows the velocity overshoot that coincides with the ring-to-point transition. Arrows A and B correspond to the first and last data points in the inset; (b) Numerical prediction of steady-state defect positions for $A = 30$, after Fig. 7 of [Zhou et al. 2007], ©Cambridge University Press.

3.3 *Air bubbles in motion*

In another series of experiments, we study the rise of air bubbles in the liquid crystal cell. An advantage of using air bubbles is the significantly higher density difference; it is around 1.0 g/cc compared to 0.1 g/cc for oil-5CB system. This will result in higher Ericksen numbers for which it will be interesting to see how the flow affects the defects. Typical bubble diameters for various runs are in the range of 100 to 250 μm . It now becomes more difficult to capture the initial moments of bubble rise due to disturbance caused by the capillary and also the bubble's rapid acceleration. There is visual evidence of an initial ring quickly converging to a point defect as the bubble accelerates, but it is not enough to yield a complete data set such as in Figure 21(a). Rather, we focus on the later stages of the bubble's rise.

We observe that once the point defect is formed, it gets convected farther downstream and leads to the formation of a long tailed loop which appears bright against the dark background, under crossed polarizers, as shown in inset B2 of Figure 22. We must note here that the loop appears bright due to the tilt of director away from either polarizers' axis; it is not a defect loop by itself. Rather, the point defect is located at the tip of the terminating loops as has been verified by computations (inset C). Away from the rising bubble this loop narrows down to eventually terminate to a point, which is similar to the bright lobes of an oil drop with hyperbolic point defect (Figure 17(b)), but elongated up to $20a$ at the highest bubble speed. The loop remains of approximately constant length as long as the rise velocity does not change much. Now, as the rise velocity starts to decrease, we note that the loop starts shrinking towards the bubble interface and the point defect moves closer. A further reduction in velocity ensures more retraction (inset B1), and finally at near static state, the bubble seems to develop a stable point defect very close to its interface (inset A). It reverts to the relatively broad bright lobes as the bubble comes to a stop. The point defect may remain indefinitely but sometimes opens into a Saturn ring as illustrated in Figure 19.

For bubble radius on the order of 60 μm , the elastic relaxation time is $\eta\alpha^2/K \approx 28$ s. The entire rise takes some 200 seconds, and cannot be considered quasi-static. This implies that the defect configuration at any particular time is undergoing relaxation and is dependent on the history up to that point, and there is no one-to-one correlation between r_d and the instantaneous bubble

velocity or Er . The scatter among different runs reflects the fact that transient effects due to elastic relaxation and history are at play. Nevertheless, the positive slope of the data, in both the accelerating and decelerating stages, is consistent with the steady-state computations of Zhou et al. [2007], although the experimental r_d values are much higher than the computed ones for the same Er . Aside from the aforementioned transient effects and the mismatched A ($A \approx 60$), the experimental geometry is more complex than the axisymmetric computational domain, and the close proximity of the cell walls may also have contributed to the elongated loop.

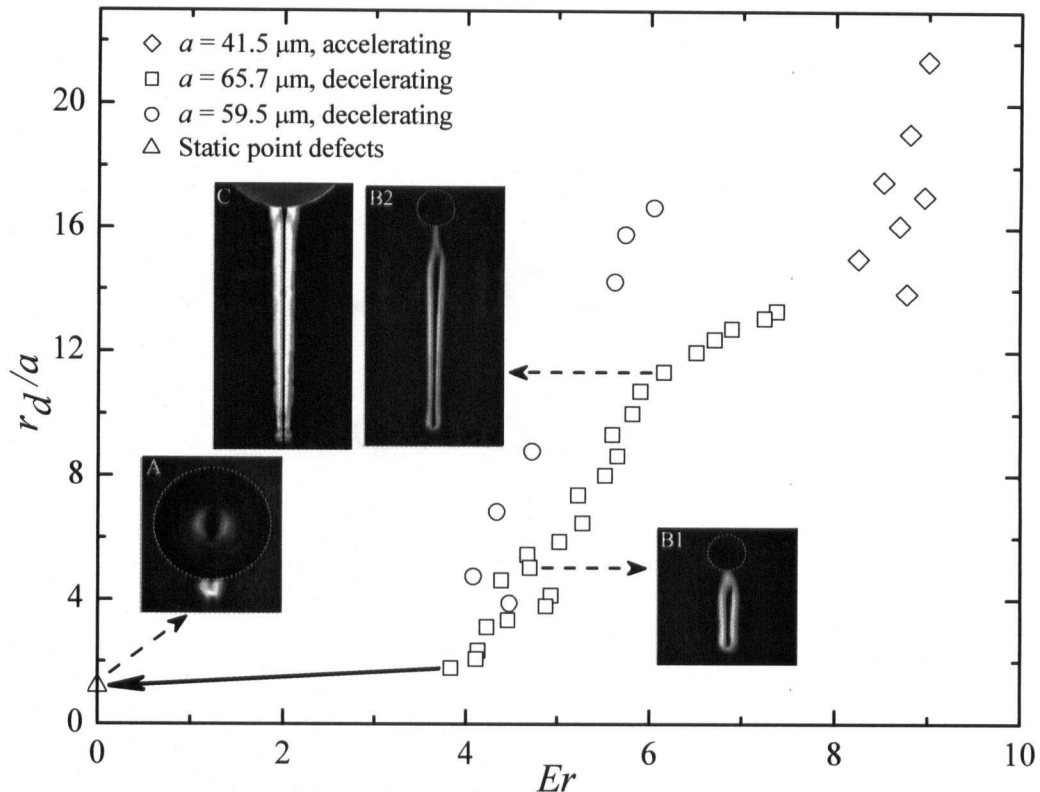


Figure 22: Position of the point defect as a function of the instantaneous Ericksen number (Er) for accelerating and decelerating bubbles. Insets B1 and B2 show the bright birefringent loops with the point defect at the bottom, and inset C shows a computed^{†††} birefringent pattern roughly corresponding to B2. The solid arrow indicates the final stabilization of the point defect to its equilibrium position (inset A).

^{†††} Computation by C. Zhou.

3.3.1 Elastic relaxation

At times the convected loop elongates enough (see Figure 23(a)), so that when the bubble stops completely we observe pure elastic relaxation of the loop. Figure 23 (b)-(e) shows the further retraction in process. Initially the point defect retreats with an instantaneous velocity $v_{\text{loop}} \approx 17.6 \mu\text{m/s}$ which later decreases to $0.7 \mu\text{m/s}$ close to the bubble surface. This indicates the presence of a force-distance type relationship, the force becoming weaker with decreasing distance.

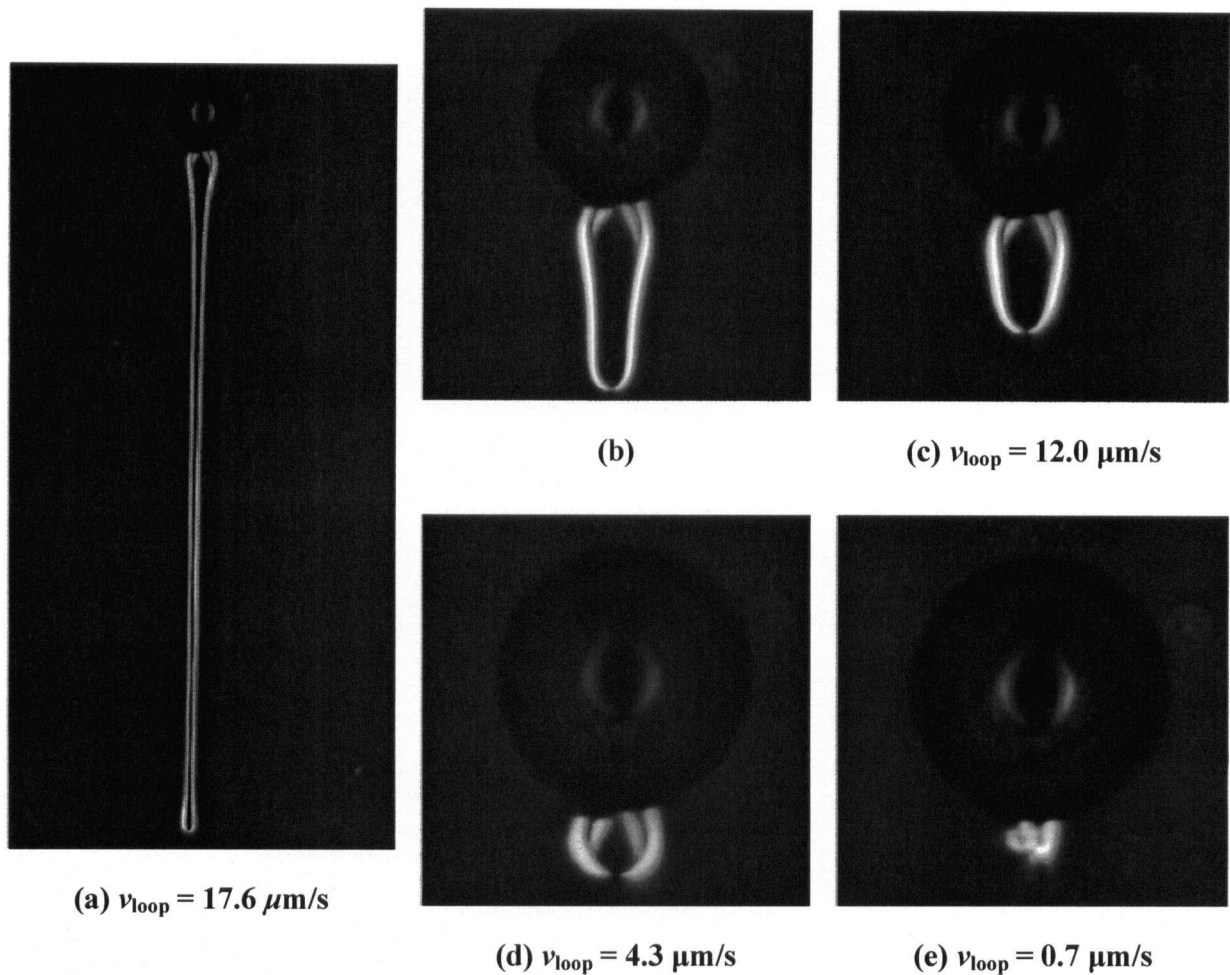


Figure 23: Time series (a) - (e) of the elastic retraction process on a static bubble. The instantaneous loop retraction velocities (v_{loop}) are given except for (b) which is the start of a new reference frame.

3.3.2 Loop breaking

Occasionally, the elongated loop gets twisted and then breaks off at the point of crossover, leading to the formation of a stand-alone loop bearing a point defect at each end. The twin point defects then annihilate each other as shown in the sequence of Figure 24. The speed of retraction of each point defect is $13.7 \mu\text{m/s}$; on the same order as the defect retraction speed near a bubble (cf. Figure 23).

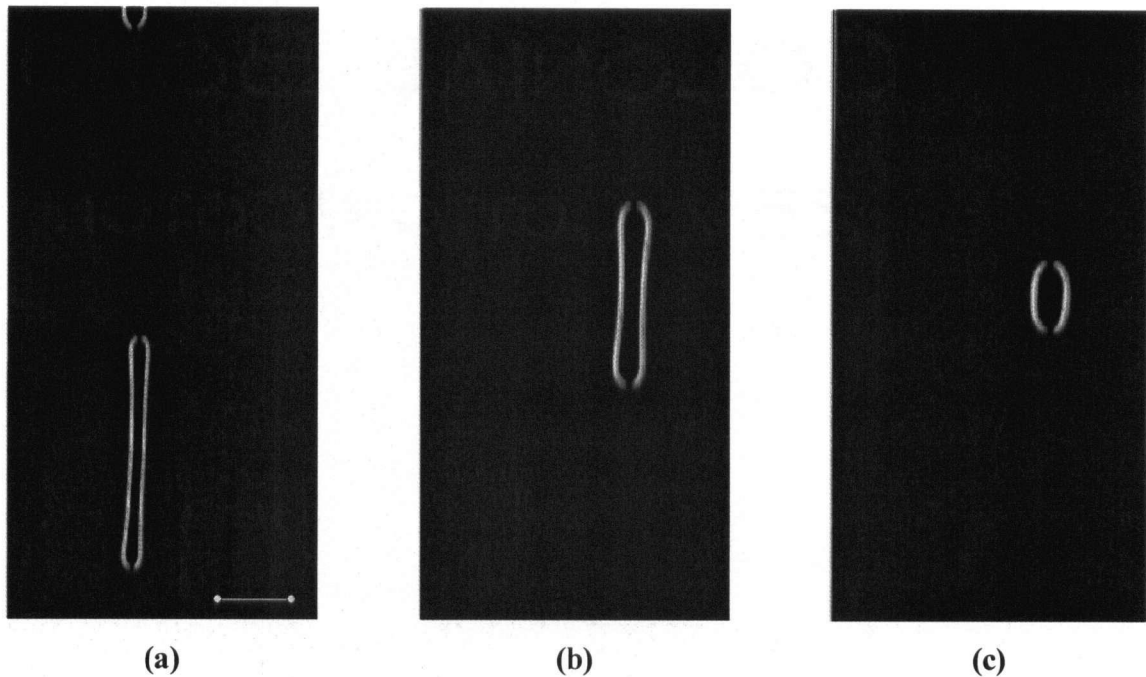


Figure 24: Annihilation of a pair of opposite point defects with opposite charges. The length of the loop shrinks at a rate of $27.4 \mu\text{m/s}$, so that each point defect moves at a speed of $13.7 \mu\text{m/s}$. The scale bar in (a) corresponds to $100 \mu\text{m}$.

3.4 *Multi particle interactions*

3.4.1 Self assembly among micro-droplets and micro-bubbles

Colloidal systems can be defined as the suspension of small particles of one component in bulk phase of another component. In general, the size of particles is small enough for surface effects to dominate over bulk effects. Hence, the particle-particle and particle-fluid interaction in these systems crucially depends upon surface tension, electrostatic and dipolar interactions and van der Waals interactions among other quantities. Their importance can be judged from the wide range of applications in food industry, pharmaceuticals, agrochemicals, paints and coatings, printing inks, and even cosmetics.

Dispersions in a liquid crystalline medium are unique owing to the presence of additional mediators like elastic forces due to the anisotropy of the medium. These suspended droplets are each accompanied by a companion hyperbolic hedgehog defect. However, the presence of multiple droplets leads to interesting colloidal interactions. A delicate balance between the attractive and repulsive forces leads to a chaining phenomenon also known as self-assembly. Poulin et al. [1997] observed this for an emulsion of water droplets in 5CB stabilized by surfactants. Their small ($<5 \mu\text{m}$) water droplets formed linear chains at the center of bigger nematic drops suspended in water. These chains of droplets stabilize at fixed inter-particle distances (close to the droplet radius) in accordance with the minimisation of energy. All of their observed droplets seemed to accompany a hyperbolic hedgehog defect. Further, phase separation mechanism has proved quite useful to generate colloidal solutions of micro-droplets. Very long chains of highly ordered monodisperse oil droplets have been observed to form in aligned liquid crystal [Loudet 2005].

This phenomenon of self-assembly was also observed in our experimental system. Figure 25 shows one such example of supra-micron sized oil droplets self assembling into a linear chain. Contrary to prior observations, our dispersed oil droplets are not only accompanied by the hyperbolic hedgehog defect, but are often coupled with quadrupolar defects as well (Figure 25). It is difficult to ascertain whether these are indeed Saturn-rings because of the low optical resolution. Further, the self-assembly phenomenon was also found to occur at a larger scale of particle diameters ($\approx 100 \mu\text{m}$). A collection of air bubbles exhibited a range of defect interactions

as they self-assembled over a period of few minutes. A snapshot of the self-assembled segment of air bubbles is shown in Figure 26.

These observations indicate the presence of a broad range of conditions under which particles can self-assemble in an anisotropic medium.

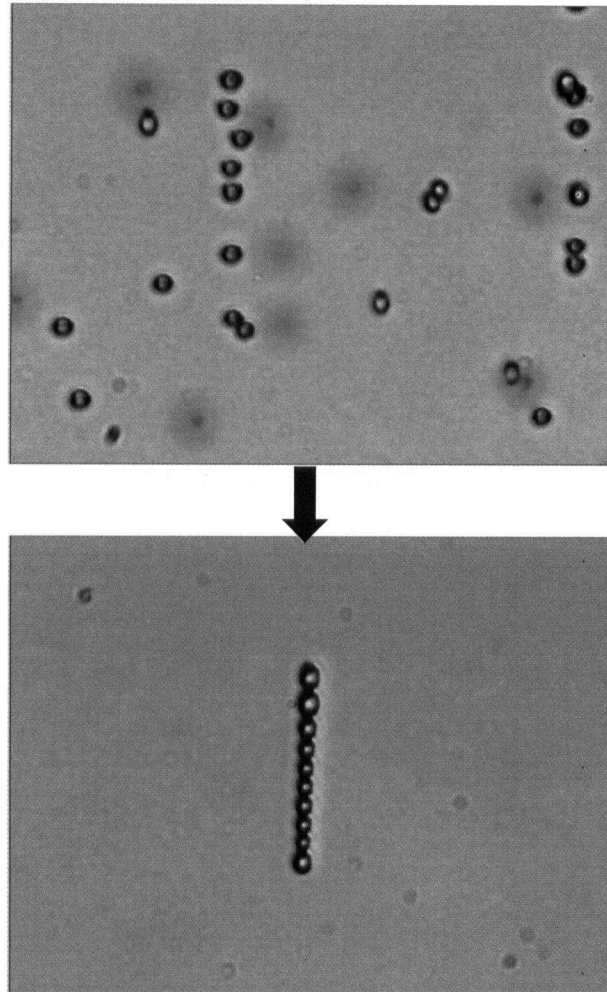


Figure 25: Self-assembly of oil droplets in LC medium. The droplets are in the size range of ≈ 5 to 10 microns.

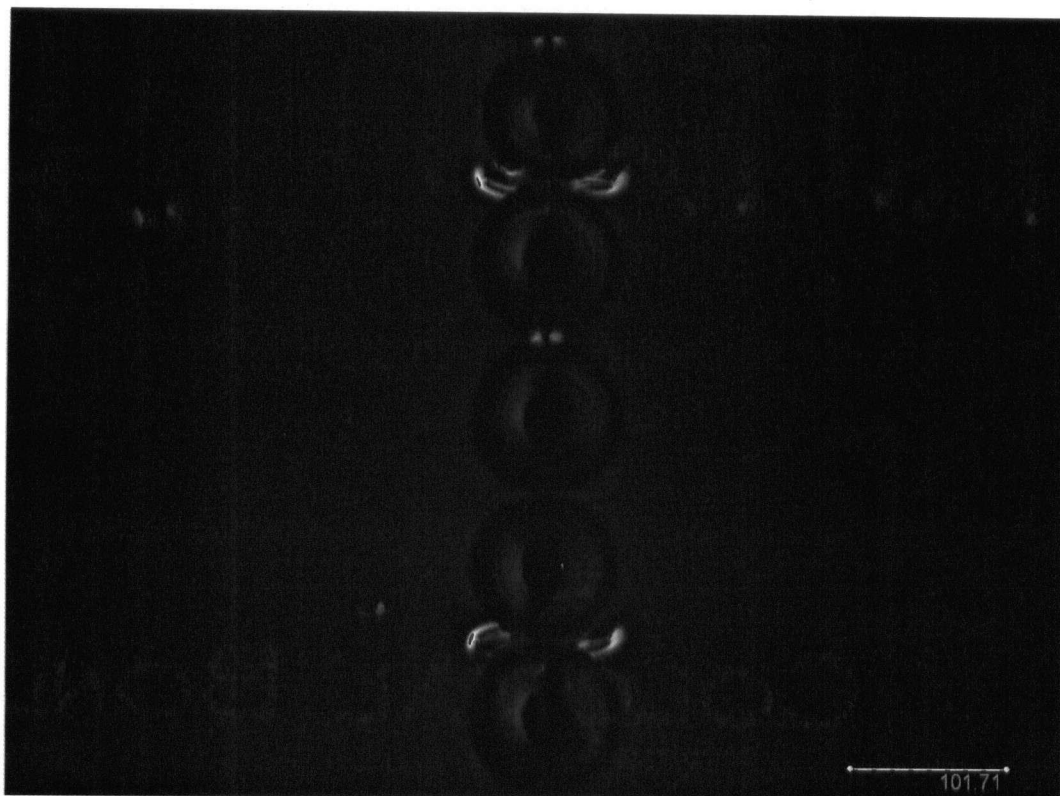


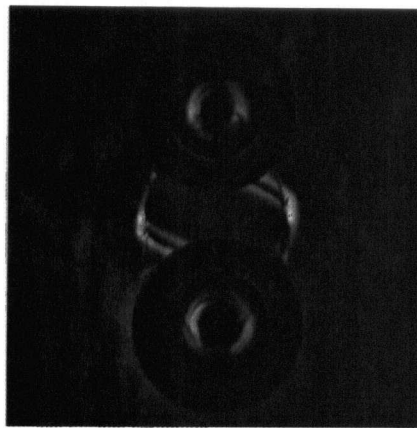
Figure 26: Self assembly at a large scale. Air bubbles, $\approx 100 \mu\text{m}$ in diameter, self assembling in vertically aligned liquid crystal.

3.4.2 Deformed defect structures

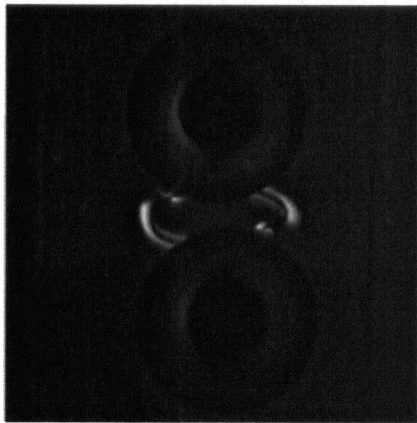
Besides the aforementioned satellite point and Saturn-ring defects, other distinctive defect configurations were also observed. The most notable one among these is the formation of a twisted dipolar type structure in between two droplets as shown in Figure 27(a) and (b). One possible explanation could be the interaction between the repulsive elastic force and attractive electrostatic force leading to two disjointed hyperbolic defects accompanying each particle. These look similar to the so-called ‘bubble-gum’ defects observed by Poulin and co-workers. On the other hand a configuration in which the director escapes in the third dimension achieving a toroidal non-topological disclination, as hypothesized in [Lubensky et al. 1998], may also lead to the observance of such pattern.

In a few other instances two bubbles separated at large distances show signs of a stretched-gum like defect (Figure 27(c)) marked by two birefringent streaks, broad near the bubble surface and narrow at the middle. The two bubbles do not seem to attract each other over a period of many

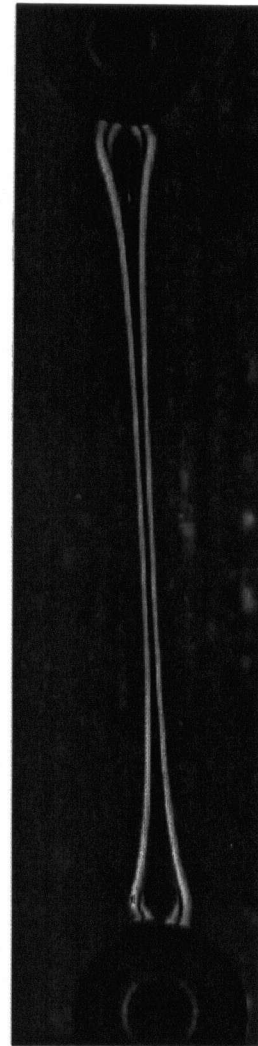
minutes. In general, an elastic force between the particles should scale as Ka^2/d^2 , a and d being the particle radius and separation. Thus, the force may be too small to create a visible motion for the separation $d \approx 10a$ in Figure 27(c). These uncommon defect structures again highlight the nontrivial nature of diverse elastic interactions that arise between particles dispersed in anisotropic media.



(a)



(b)



(c)

Figure 27: Deformed defect structure can be observed between a pair of static air bubbles in (a) and (b) above. Another pair of static bubbles (c) at separation distance $d \approx 10a$ form a stretched-gum type of defect

3.5 *Conclusions*

This study represents the first direct observation of dynamic evolution of defects near moving droplets or bubbles. It clarifies the picture suggested by prior computations and settles the controversy on the direction of convection of defects. It provides direct evidence for flow-induced ring-to-point transformation. Also, it captures the intermediate steps leading to a spontaneous point defect to Saturn-ring transition. This is unique, in that similar transitions observed previously were achieved through the use of external fields or variations in surface energy. The evidence of opening of Saturn ring in real time adds a new clue towards understanding the mechanism of defect transformation around drops and bubbles. The experiments were conducted with a nematic liquid crystal (5CB) but the results obtained are expected to be rather general. They are in good agreement with previous theoretical calculations, which are based on a general constitutive model over a moderate range of parameters.

Insomuch as defects mediate the interaction among particulates in nematic media, the insights on defect evolution are useful for understanding pattern formation in flowing nematic colloids and dispersions. Moreover, the flow field may be used as a means to manipulate defect location and configuration near isotropic-nematic interfaces, as electric and magnetic fields have been in the past, leading to potential industrial applications. It provides a new insight into the dynamics of defect structures and offers hope of new ways to manipulate, control and understand the evolutionary mechanism of defects accompanying particles in motion. Liquid crystals provide an excellent medium for attaining ordered polymeric nanostructures as has been demonstrated by the phenomenon of self-assembly. Following are some examples of current and potential applications involving liquid crystals [Date et al. 1998; Drzaic 2006; Hegmann et al. 2007]:

- ‘Filled nematics’, which contain suspensions of fine particles in a nematic liquid crystal, create intensive light scattering due to the presence of a large number of defects. A sandwiched film of such material becomes transparent in the presence of an electric field due to alignment of the LC molecules with the field. However, these filled nematics show residual transmittance even after the field is switched off leading to memory effect. This can lead to potential applications in optical storage.

- Polymeric Dispersed Liquid Crystals (PDLCs) are being developed for their use as light shutters and switchable privacy windows. PDLCs consist of micro-droplets of liquid crystal phase dispersed in a polymer matrix sandwiched between two glass plates. When no electric field is applied, the randomly oriented liquid crystal droplets scatter light to create an opaque state. However, when an electric field is applied, it orients the director parallel to the field allowing light transmission which makes it transparent.
- Liquid crystals have been employed for testing semiconductors to locate defects which generate heat and in analyzing power distribution in semiconductor devices.
- The use of liquid crystals is being actively explored in high density optical storage, recording media (electronic paper), projection light valves (for replacing current LCDs), as solvents in NMR studies and as spatial light modulators (using ferroelectric liquid crystals).

3.6 Recommendations for future work

Although the present results provide considerable new insights on defect evolution around drops and bubbles moving in nematic liquid crystals, there are still issues to be clarified by further research. The following are some suggestions and comments:

1. The data set for air bubbles, on Ericksen numbers greater than the critical value at which the ring turns into a point defect downstream, can be made more comprehensive and comparable by accounting for the 'history-effect'. One possible way to achieve this is to conduct large number of runs with longer rise times so that it can approach quasi-static behaviour.
2. On a similar note, to bridge the gap between the Ericksen numbers near ring to point defect transition and the downstream convection of the point defect, materials yielding lower rise velocities could be used. For example, using oils of greater density differences resulting in intermediate Ericksen numbers can give a data set that fits in between the current oil and bubble runs.

3. The effect of the proximity of the bounding walls on the stability of defect types can be explored further. As has already been analysed theoretically [Grollau et al. 2003], confinement enhances the stability of Saturn-ring defects. Experiments can be done to determine the exact nature of the relationship of defect stability to confinement. This may prove as a useful mediator for spontaneous transitions between defects.

4. The presence of multiple particles in liquid crystalline medium can generate a range of possible interactions. For example, particles accompanied by dipolar point defects have long range attractive and short range repulsive forces, as seen by the self-assembly phenomenon. A more careful examination of this behaviour can establish the nature of force-distance relationship that exists with different types of defects.

4 REFERENCES

- Chandrasekhar, S. (1992). Liquid Crystals. Cambridge, Cambridge University Press.
- Chuang, I., R. Durrer, N. Turok and B. Yurke (1991). "Cosmology in the Laboratory - Defect Dynamics in Liquid-Crystals." Science **251**(4999): 1336-1342.
- Cognard, J. (1982). "Alignment of Nematic Liquid Crystals and their Mixtures." Molecular Crystals and Liquid Crystals: 1-77.
- Collings, P. J. and M. Hird (1997). Introduction to Liquid Crystals: Chemistry and Physics, Taylor & Francis Ltd.
- Cummins, P. G., D. A. Dunmur and D. A. Laidler (1975). "Dielectric Properties of Nematic 4'n-Pentylcyanobiphenyl." Molecular Crystals and Liquid Crystals **30**(1-2): 109-123.
- Date, M., Y. Takeuchi and K. Kato (1998). "A memory-type holographic polymer dispersed liquid crystal (HPDLC) reflective display device." Journal of Physics D: Applied Physics **31**: 2225-2230.
- de Gennes, P. G. and J. Prost (1993). The Physics of Liquid Crystals. New York, Oxford.
- Demus, D., J. Goodby, G. W. Gray, H. W. Spiess and V. Vill (1999). Physical Properties of Liquid Crystals, Wiley-VCH.
- Drzaic, P. (2006). "Putting liquid crystal droplets to work: a short history of polymer dispersed liquid crystals." Liquid Crystals **33**(11-12): 1281-1285.
- Durand, G., L. Leger, F. Rondelez and M. Veyssie (1969). "Quasielastic Rayleigh Scattering in Nematic Liquid Crystals." Physical Review Letters **22**(25): 1361.
- Feng, J. J. and C. Zhou (2004). "Orientational defects near colloidal particles in a nematic liquid crystal." Journal of Colloid and Interface Science **269**: 72-78.
- Friedel, J. (1964). Dislocations, Oxford, New York, Pergamon Press.
- Gannon, M. G. J. and T. E. Faber (1978). "The surface tension of nematic liquid crystals." Philosophical Magazine A **37**: 117-135.
- Goldman, R. D. and D. L. Spector (2005). Live cell imaging : a laboratory manual, Cold Spring Harbor, N.Y.
- Grollau, S., N. L. Abbott and J. J. de Pablo (2003). "Spherical particle immersed in a nematic liquid crystal: Effects of confinement on the director field configurations." Physical Review E **67**(1): 011702.
- Gu, Y. and N. L. Abbott (2000). "Observation of Saturn-Ring Defects around Solid Microspheres in Nematic Liquid Crystals." Physical Review Letters **85**(22): 4719-4722.

- Guang, M. and O. Rudolf (1994). Fast imaging polarimetry with precision universal compensator, SPIE.
- Hegmann, T. (2007). "Nanoparticles in Liquid Crystals: Synthesis, Self-Assembly, Defect Formation and Potential Applications." Journal of Inorganic and Organometallic Polymers and Materials **17**(3): 483-508.
- Kasten, H. and G. Strobl (1995). "Nematic wetting at the free surface of 4-cyano-4'-n-alkyl-biphenyls." Journal of Chemical Physics **103**(15): 6768-6774.
- Katoh, K., G. Langford, K. Hammar, P. J. S. Smith and R. Oldenbourg (1997). "Actin bundles in neuronal growth cone observed with the pol-scope." Biological Bulletin **193**(2): 219-220.
- Khullar, S., C. Zhou and J. Feng (2007). "Dynamic evolution of topological defects around drops and bubbles rising in a nematic liquid crystal." Physical Review Letters (submitted).
- Kleman, M. and O. D. Lavrentovich (2003). Soft Matter Physics, Springer.
- Lavrentovich, O. D., V. G. Nazarenko, V. V. Sergan and G. Durand (1992). "Dielectric quenching of the electric polar surface instability in a nematic liquid crystal." Physical Review A **45**(10): R6969-R6972.
- Lavrentovich, O. D. and V. M. Pergamenschchik (1994). "Stripe Domain Phase of a Thin Nematic Film and the K13 Divergence Term." Physical Review Letters **73**(7): 979-982.
- Loudet, J. C. (2005). "Colloidal inclusions in liquid crystals: Phase separation mechanisms and some dynamical aspects." Liquid Crystals Today **14**: 1-14.
- Loudet, J. C. and P. Poulin (2001). "Application of an Electric Field to Colloidal Particles Suspended in a Liquid-Crystal Solvent." Physical Review Letters **87**(16): 165503.
- Lubensky, T. C., D. Pettey, N. Currier and H. Stark (1998). "Topological defects and interactions in nematic emulsions." Physical Review E **57**(1): 610-625.
- Mertelj, A. and M. Copic (2000). "Dynamic light scattering as a probe of orientational dynamics in confined liquid crystals." Physical Review E **61**(2): 1622-1628.
- Mondain-Monval, O., J. C. Dedieu, T. Gulik-Krzywicki and P. Poulin (1999). "Weak surface energy in nematic dispersions: Saturn ring defects and quadrupolar interactions." European Physical Journal B **12**: 167-170.
- Nabarro, F. (1967). Theory of crystal dislocations, Oxford, Clarendon P.
- Oldenbourg, R. (1999). "Polarized light microscopy of spindles." Methods in Cell Biology, Vol **61**: 175-208.
- Oldenbourg, R. and G. Mei (1995). "New Polarized-Light Microscope with Precision Universal Compensator." Journal of Microscopy-Oxford **180**: 140-147.

- Oldenbourg, R., E. D. Salmon and P. T. Tran (1998). "Birefringence of single and bundled microtubules." Biophysical Journal **74**(1): 645-654.
- Orwoll, R. A., V. J. Sullivan and G. C. Campbell (1987). "Thermal Pressure Coefficients and Specific Volumes of Cyanobiphenyls and Their Transition Entropies at Constant Volume." Molecular Crystals and Liquid Crystals **149**: 121-140.
- Porter, R. S. and K. T. Schell (1990). "Binary Phase Studies of 4-4'-N-Pentylcyanobiphenyl." Molecular Crystals and Liquid Crystals **182**: 185-194.
- Poulin, P., V. Cabuil and D. A. Weitz (1997). "Direct Measurement of Colloidal Forces in an Anisotropic Solvent." Physical Review Letters **79**(24): 4862-4865.
- Poulin, P., H. Stark, T. C. Lubensky and D. A. Weitz (1997). "Novel colloidal interactions in anisotropic fluids." Science **275**: 1770-1773.
- Poulin, P. and D. A. Weitz (1998). "Inverted and multiple nematic emulsions." Physical Review E **57**: 626-637.
- Rapini, A. and M. Papoular (1969). Journal of Physics (Paris), Colloq. **30**: C4-54.
- Ray, R. and A. M. Srivastava (2004). "Measuring cosmic defect correlations in liquid crystals." Physical Review D (Particles, Fields, Gravitation, and Cosmology) **69**(10): 103525-103510.
- Ruhwandl, R. W. and E. M. Terentjev (1997). "Monte Carlo simulation of topological defects in the nematic liquid crystal matrix around a spherical colloidal particle." Physical Review E **56**: 5561-5565.
- Sakagami, S., A. Takase and M. Nakamizo (1973). "Deformation of Molecular-Orientation of Nematic Liquid-Crystals with Homeotropic Alignment in Electric-Field." Bulletin of the Chemical Society of Japan **46**(11): 3573-3574.
- Sen, S., P. Brahma, S. K. Roy, D. K. Mukherjee and S. B. Roy (1983). "Birefringence and Order Parameter of Some Alkyl and Alkoxybiphenyl Liquid-Crystals." Molecular Crystals and Liquid Crystals **100**(3-4): 327-340.
- Stark, H. (1999). "Director field configurations around a spherical particle in a nematic liquid crystal." European Physical Journal B **10**(2): 311-321.
- Stark, H. (2001). "Physics of colloidal dispersions in nematic liquid crystals." Physics Reports **351**: 387-474.
- Stark, H. (2002). "Saturn-ring defects around microspheres suspended in nematic liquid crystals: An analogy between confined geometries and magnetic fields." Physical Review E **66**(3): 032701.
- Stark, H. and D. Venzki (2002). "Non-linear Stokes drag of spherical particles in a nematic solvent." Europhysics Letters **57**: 60-66.

Tintaru, M., R. Moldovan, T. Belca and S. Frunza (2001). "Surface tension of some liquid crystals in the cyanobiphenyl series." Liquid Crystals **28**(5): 793-797.

Tsvetkov, V. N. (1942). Acta Physicochim. USSR **16**: 132.

Vollhardt, D. (1990). The superfluid phases of helium 3, London ; New York : Taylor & Francis.

Voltz, C., Y. Maeda, Y. Tabe and H. Yokoyama (2006). "Director-Configurational Transitions around Microbubbles of Hydrostatically Regulated Size in Liquid Crystals." Physical Review Letters **97**(22): 227801.

Wu, J. and P. T. Mather (2005). "Interfacial Tension of a Liquid Crystalline Polymer in an Isotropic Polymer Matrix." Macromolecules **38**: 7343-7351.

Wu, M. H., K. Koseki and T. Amari (2003). "Electroviscous effect of nematic liquid crystals in the slit-viscometer." Thin Solid Films **438**: 396-402.

Yoneya, M., J. I. Fukuda, H. Yokoyama and H. Stark (2005). "Effect of a hydrodynamic flow on the orientation profiles of a nematic liquid crystal around a spherical particle." Molecular Crystals and Liquid Crystals **435**: 75-85.

Zhou, C., P. Yue and J. J. Feng (2007). "The rise of Newtonian drops in a nematic liquid crystal." Journal of Fluid Mechanics (submitted).

Zhou, C., P. Yue, J. J. Feng, C. Liu and J. Shen (2007). "Heart-shaped bubbles rising in anisotropic liquids." Physics of Fluids **19**: 041703.

5 APPENDIX

5.1 Structure and properties of 5CB

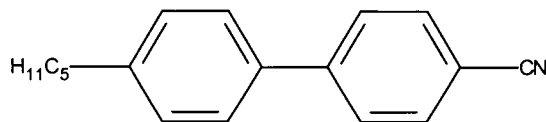


Figure 28: Molecular representation of liquid crystal 5CB

Formula: C₁₈ H₁₉ N₁

Mass: 249.359 g/mol

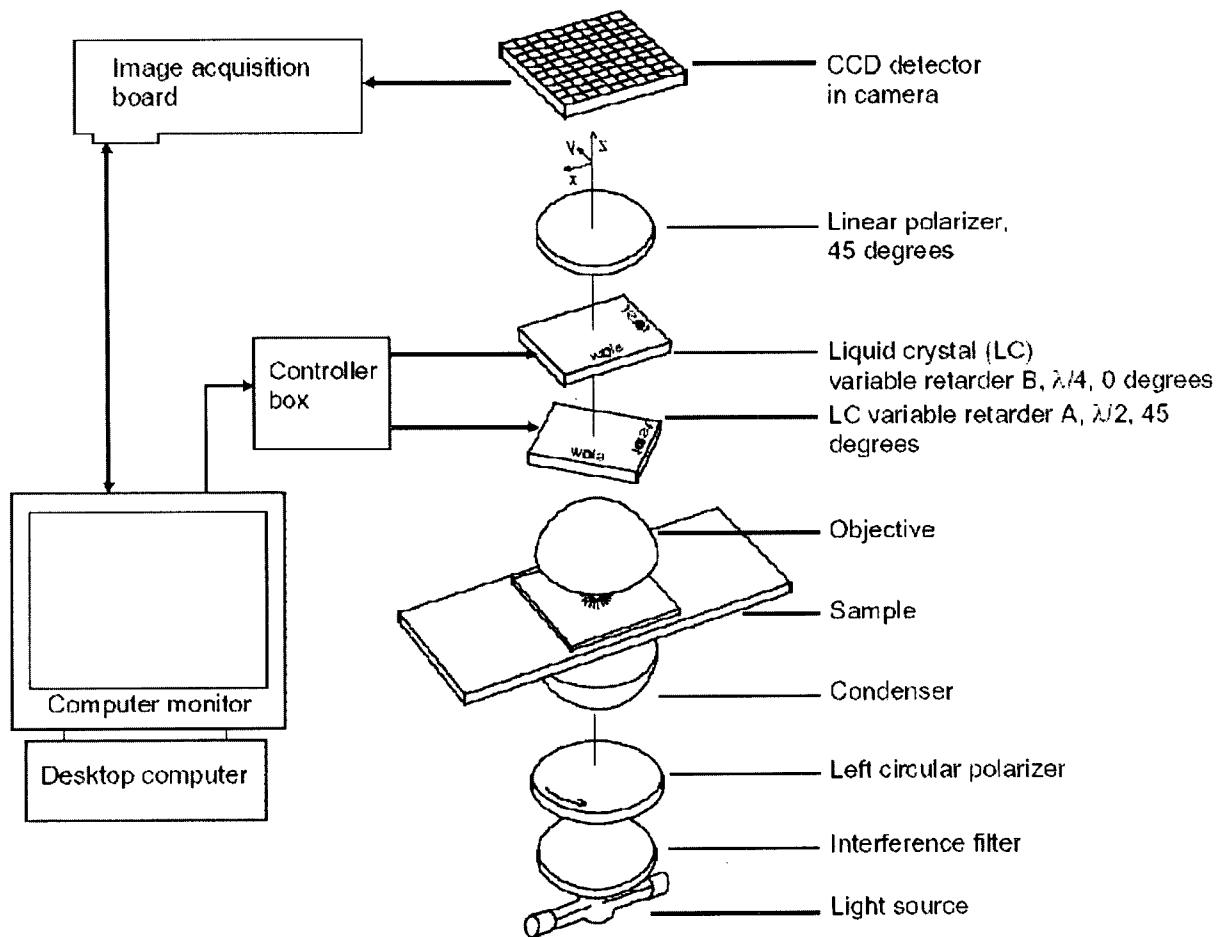
IUPAC Name: 4'-Pentyl-4-biphenylcarbonitrile

Phases: Cr 23 N 35.3 I

Table 2: Additional properties of 5CB

Category/Property	Value	Reference
Thermo	$\Delta H(\text{N-is})$ 0.39 kJ/mol, $T = 35.2$ °C	[Orwoll et al. 1987]
	$\Delta H(\text{Cr-N})$ 15.7 cal/g, $T = 22.3$ °C	[Porter and Schell 1990]
Optics	$n_e = 1.6975$, $T=24$ °C	[Sen et al. 1983]
	$n_o = 1.53$, $T=25$ °C	[Cummins et al. 1975]
Density	$\rho = 1.008$ g/cm ³	Sigma-Aldrich

5.2 *Abrio's Working Layout*



5.3 *Abrio's Specifications*

Optics	
Wavelength of Operation	546 nm
Spatial Resolution	Diffraction limited
CCD Camera	
Chip Dimensions	2/3-inch diagonal
Image Size	1392 x 1040
Pixel Dimensions	6.47 x 4.83 μm
Environmental Requirements	
Operating temperature	15 °C to 40 °C
Operating humidity	65%, non-condensing